International Journal of Nanomedicine

Dovepress
open access to scientific and medical research

Open Access Full Text Article

ORIGINAL RESEARCH

Delivery of Avocado Seed Extract Using Novel Charge-Switchable Mesoporous Silica Nanoparticles with Galactose Surface Modified to Target Sorafenib-Resistant Hepatocellular Carcinoma

Aalok Basu[1], Arunsajee Sae-be[1], Thanaphon Namporn[1], Orasa Suriyaphan[2], Pongtip Sithisarn[3], Jiraporn Leanpolchareanchai[1], Piyaporn Plommaithong[1], Apichat Chatsukit[1], Khanit Sa-ngiamsuntorn[4], Parichart Naruphontjirakul[5], Pakatip Ruenraroengsak[1,6]

[1]Department of Pharmacy, Faculty of Pharmacy, Mahidol University, Bangkok, Thailand; [2]Department of Food Chemistry, Faculty of Pharmacy, Mahidol University, Bangkok, Thailand; [3]Department of Pharmacognosy, Faculty of Pharmacy, Mahidol University, Bangkok, Thailand; [4]Department of Biochemistry, Faculty of Pharmacy, Mahidol University, Bangkok, Thailand; [5]Biological Engineering Program, Faculty of Engineering, King Mongkut's University of Technology Thonburi, Bangkok, Thailand; [6]Centre of Molecular Targeting and Integrated Drug Development, Faculty of Pharmacy, Mahidol University, Bangkok, Thailand

Correspondence: Pakatip Ruenraroengsak, Division of Pharmaceutical Technology, Department of Pharmacy, Faculty of Pharmacy, Mahidol University, 447 Sri-Ayuthaya Road, Rajathevi, Bangkok, 10400, Thailand, Email pakatip.rue@mahidol.ac.th

Background: Sorafenib-resistant (SR) hepatocellular carcinoma (HCC) is a current serious problem in liver cancer treatment. Numerous phytochemicals derived from plants exhibit anticancer activity but have never been tested against drug-resistant cells.

Methods: Avocado seed extract (APE) isolated by maceration was analysed for its phytochemical composition and anticancer activity. Novel design charge-switchable pH-responsive nanocarriers of aminated mesoporous silica nanoparticles with conjugated galactose (GMSN) were synthesised for delivering APE and their physicochemical properties were characterized. The drug loading efficiency (%LE) and entrapment efficiency (%EE) were evaluated. Anticancer activity of APE loaded GMSN was measured against HCC (HepG2, Huh-7) and SR-HCC (SR-HepG2).

Results: Anticancer activity of APE against non-resistant HepG2 (IC_{50} 50.9 ± 0.83 μg mL^{-1}), Huh-7 (IC_{50} 42.41 ± 1.88 μg mL^{-1}), and SR-HepG2 (IC_{50} 62.58 ± 2.29 μg mL^{-1}) cells was confirmed. The APE loaded GMSN had a diameter of 131.41 ± 14.41 nm with 41.08 ± 2.09%LE and 44.96 ± 2.26%EE. Galactose functionalization (55%) did not perturb the original mesoporous structure. The GMSN imparted positive surface charges, 10.3 ± 0.61mV at acidic medium pH 5.5 along with rapid release of APE 45% in 2 h. The GMSN boosted cellular uptake by HepG2 and SR-HepG2 cells, whereas the amine functionalized facilitated their endosomal escape. Their anticancer activity was demonstrated in non-resistant HCC and SR-HCC cells with IC_{50} values at 30.73 ± 3.14 (HepG2), 21.86 ± 0.83 (Huh-7), 35.64 ± 1.34 (SR-HepG2) μg mL^{-1}, respectively, in comparison to the control and non-encapsulated APE.

Conclusion: APE loaded GMSN is highly effective against both non-resistant HCC and SR-HCC and warrants further *in vivo* investigation.

Keywords: liver cancer, hepatocellular carcinoma, galactose, sorafenib drug resistance, avocado, mesoporous silica nanoparticles

Introduction

According to the World Health Organization, primary liver cancer is the sixth most common cancer and is expected to affect more than 1.4 million people by 2040. Hepatocellular carcinoma (HCC) is a major category of liver cancer, accounting for 80–90% of liver cancer cases globally, with high morbidity and mortality.[1] Early detection systems of HCC through ultrasonography and serological tests of α-fetoprotein have remained limited due to insensitivity and false-positive results.[2] Therefore, most HCC patients diagnosed at advanced stages must rely on a chemotherapy.[3,4] Although combinations of tyrosine kinase inhibitors, such as sorafenib, and immunotherapy have been approved to handle advanced stages of the disease, their clinical outcomes are unsatisfactory, with an overall survival benefit of approximately 13.6 months.[5]

Received: 28 June 2024
Accepted: 14 September 2024
Published: 14 October 2024

Graphical Abstract

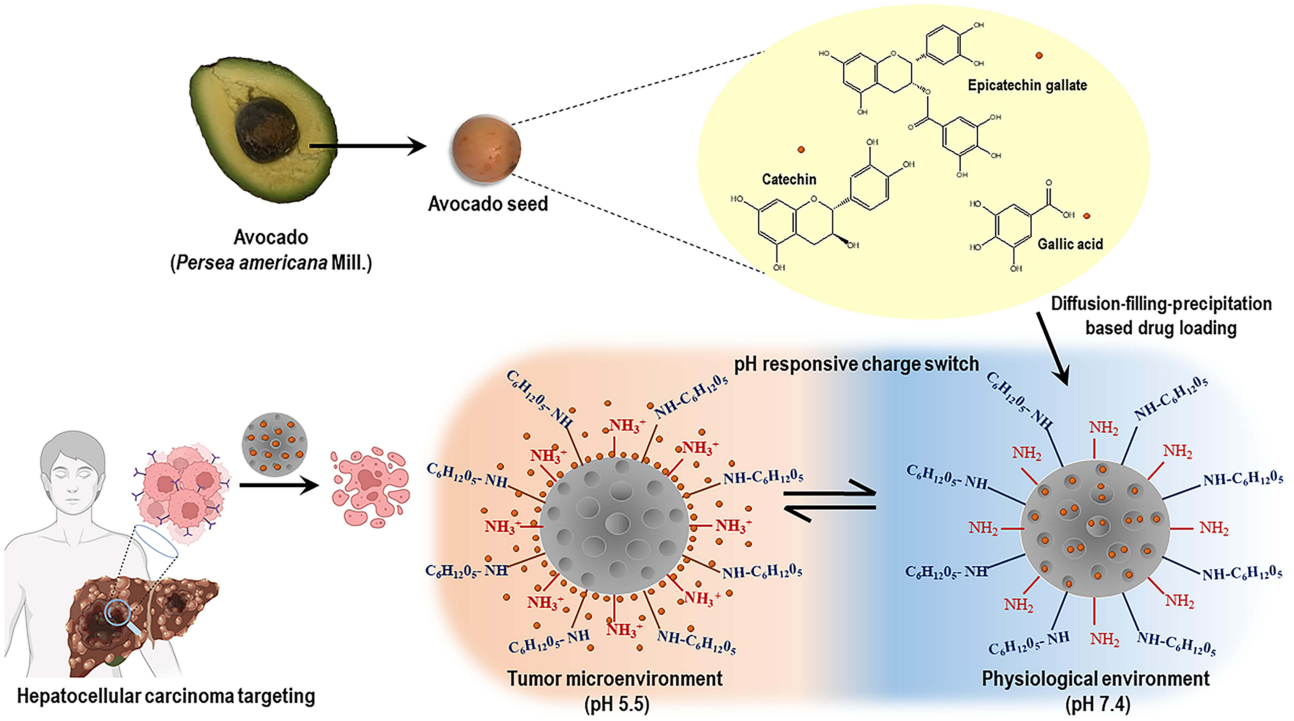

Furthermore, HCC steadily develops resistance to first-line drugs, such as docetaxel, lenvatinib, cabozantinib, and sorafenib, leading to an increase in the HCC recurrence rate at local and distant sites.[6,7] Although strategies such as immune checkpoint blockage and CRISPR/Cas9 genome editing look promising for HCC therapy, they are still at their infancy.[8,9] Consequently, the next generation of anti-HCC molecules together with urgent interventions for their specific delivery are required to raise the number of HCC survival cases.

It has been estimated that more than 1.3 billion tons of agro-industrial waste including seed, pulp, leaf, stem, and bark, are discarded each year.[10] Recent works in drug discovery and complementary medicines have demonstrated that procyanidins,[11,12] derived from grape seeds and other agro-industrial wastes, exert anticancer effects through multiple pathways, but the ability to be formulated and tested against HCC models has largely been neglected.[13] Avocado (*Persea americana* Mill.) or alligator pearl is one of the most nutritious commercial fruits and exhibits various pharmacological activities, including antioxidant, analgesic, hypoglycaemic, and anticancer activities.[14–16] While the pulp is consumed worldwide, the seed (representing approximately 30% of the whole fruit) is commonly considered as waste.[17] The therapeutic value of avocado as an aphrodisiac has been identified since the Mayan and Aztec civilisations.[18] However, only the few studies have focused on the anticancer effects of avocado seed extracts. Dabas et al[19] showed that ethanolic extracts of avocado seeds exhibited 50% inhibitory concentration (IC_{50}) values of 99.7 μg mL^{-1} in MCF7 human breast cancer cells. Both aqueous and ethanolic extracts proved to be effective against the breast cancer cell-line T47D, with rather high IC_{50} values of 560.2 μg mL^{-1} and 107.2 μg mL^{-1}. In 2019, Elhalwagy et al[15] reported that avocado seed lipid extracts could be a superior alternative to sorafenib in the treatment of liver cancer. However, the study lacked in-depth information on phytochemical profiles, presence of major bioactive compounds, and anticancer mechanisms. Phytochemical studies revealed that the avocado seeds contain a number of extractable bioactive compounds, including polyphenols and procyanidins (such as catechin and epicatechin), all of which can be explored as viable strategies to modulate tumorigenesis and their underlying signalling pathways.[20] Moreover, these compounds demonstrated the potential to overcome drug resistance through inhibition and downregulation of P-glycoprotein.[21] Avocado seed wastes may thereby be employed as an

inexpensive and sustainable source of procyanidins for a new generation anticancer therapy. It is also worth investigating whether avocado seed extract (APE) could be a new paradigm for drug-resistant HCC therapy.

Poor aqueous solubility and physicochemical instability have been highlighted as major constraints to the use of plant-derived bioactive compounds in translational medicine. Although many strategies for tumour targeting and programmed release of plant extracts using nanocarriers have been devised,[22–26] each of them has its own limitations that are extensively detailed in our previous work.[13] Mesoporous silica-based nanomaterials have garnered considerable attention as drug carriers owing to their unique properties, including large surface area, adjustable pore size, and large pore volumes to facilitate high drug loading.[27] They are also biocompatible[28] and can be strategically modified using small molecules, stimuli-responsive polymers, and nano-gatekeepers to achieve site-specific targeting and controlled release.[29,30] Despite their interesting properties, mesoporous silica nanoparticles have seldom been used as carriers for bioactive plant compounds.

In cancer pathophysiology, the concept of "tumour microenvironment (TME) responsive drug delivery strategies" is in recent focus. In comparison to cell-specific drug delivery, TME-responsive drug delivery systems are triggered by acidic pH, enzymes, and hypoxia, and can overcome tumour heterogeneity to ensure precise delivery of cargo molecules, especially in drug-resistant conditions.[31,32] However, this system is firstly required to identify the target cells from their neighbours, followed by nanoparticle uptake. Previously, several groups have demonstrated that galactose can act as a beacon towards asialoglycoprotein receptors (ASGPR) that overexpress in HCC cells.[33] Galactose has been installed as a targeting ligand on the surface of different nanostructures, including polymeric gene vectors, pH-sensitive micelles, and nanogels.[34–36] The high binding affinity of galactose to ASGPR initiates the internalisation of nanoparticles via clathrin-mediated endocytosis that promotes cell-specific drug delivery with minimum cytotoxicity.[37] On the other hand, the presence of positively charged amino groups on the surface of mesoporous silica nanoparticles has regulated pH-responsive drug release and promotes adsorptive endocytosis via interactions with negatively charged cell membranes.[38] Numerous surface-modification reactions have employed amino groups as the arm to anchor aldose molecules on the outer surface.[39,40] Here, we conjugated galactose, a targeting ligand, to the amine-surface-modified nanoparticles and designed a new class of charge-switchable nanoparticles, especially for the delivery of APE. In this class, a certain number of amino groups are glycosylated to provide targetability, whereas others would remain available for pH-responsive behaviour. At physiological pH, the negative surface charge would predominate to improve the stability of the nanoparticles. Nonetheless, owing to the charge-switchable nature, once in TME at pH between 6.5 and 6.9, the surface charge switches to positive and triggers the rapid release of APE specifically at the tumour target site. It is hypothesized that the developed charge-switchable designed nanoparticles will enhance penetration in the TME and minimise the chances of drug resistance because the high drug concentrations can be maintained at the target sites.[41]

APE was isolated, and its phytochemical and anticancer activities were evaluated. Novel pH-responsive charge-switchable nanocarriers were designed, and their specific targeting abilities were initiated. Mesoporous silica nanocarriers with amine surface functionalization (MSN-NH_2) were synthesised. Precise control of galactosylation on the surface of MSN-NH_2 nanoparticles (GMSN) resulted in surface-charge reversal ability which could further modulate drug release in response to a specific pH. The APE loading into GMSN (GMSN@APE) was further optimised to facilitate the maximum release capacity under the sink conditions. The APE release from both MSN-NH_2 loaded APE (MSN-NH_2@APE) and GMSN@APE was quantified and compared for their loading capacity and encapsulation efficiency. Nanoparticle internalisation and endocytosis in non-resistant HepG2 and sorafenib-resistant HepG2 cells were evaluated. Anticancer activity was subsequently assessed using cell-based assays to characterize the therapeutic behaviour of the developed charge-switchable mesoporous silica nanoparticles with modified galactose surfaces.

Experimental

Materials

Ethanol for extraction (99.8%) was obtained from Merck (Sigma-Aldrich, USA). Tetraethyl orthosilicate (TEOS 98%), cetyltrimethylammonium bromide (CTAB), 3-aminopropyltriethoxysilane (APTES), galactose, fluorescein isothiocyanate (FITC), and sodium cyanoborohydride were purchased from Sigma-Aldrich (USA). The p-dimethylaminocinnamaldehyde

(DMACA) and standard compounds such as catechin, epicatechin, procyanidin B1, and B2 for procyanidin assays were also obtained from Sigma Aldrich. Sodium hydroxide pellets were purchased from Merck. Dulbecco's modified Eagle's medium (DMEM), penicillin–streptomycin (10,000 U/mL), fetal bovine serum (FBS), and trypsin-EDTA for cell cultures were purchased from Cytiva (GE Healthcare, USA). Cell proliferation (WST-1) and lactate dehydrogenase (LDH) assay kits were obtained from Roche (Germany). Human hepatoma cell lines HepG2 and Huh-7 were purchased from the Japanese Collection of Research Bioresources Cell Bank (JCRB). Water (resistivity 18.2 milliohm centimetre (mΩ·cm) at 25 °C) used for nanoparticle synthesis was purified using a Millipore Synergy UV system (Merck, USA).

Preparation of Avocado Seed Extract

Avocado fruits (*Persea americana*, family Lauraceae, Hass cultivar) grown in Australia were purchased from a wholesale distributor in Thailand. The fruit specimen was identified by Dr Sunisa Sangvirotjanapat, botanical taxonomist at Sireeruckhachati Nature Learning Park at Mahidol University, Nakhon Pathom, Thailand, and voucher specimen number was PBM 005998–006000. The fruits were allowed to ripen in a dark room at room temperature (25 ±4 °C) and were washed with water several times before processing. The seeds were manually separated from the fruits, dried in a hot-air oven at 50 ± 2 °C for 24 h, and ground into a fine powder. Forty grams of extract powder were sieved and extracted with 400 mL of a water-ethanol mixture (50:50, v/v) for 24 h at 37 ± 2 °C. The filtered menstruum was concentrated under reduced pressure and freeze-dried (Alpha 1–4, Martin Christ, Germany) to obtain a powdered extract. The freeze-dried powder was collected, packed in light-proof containers, and stored at 4 ± 2 °C until further use.

Phytochemical Evaluations

Total Polyphenol Content

Total polyphenols in the APE were quantified following the method described by Pongtip et al.[42] Briefly, 25 µL of extract (containing 1 mg mL^{-1}) was mixed with 25 µL Folin-Ciocalteu reagent, followed by 75 µL water and 100 µL sodium carbonate (20%, w/v). The mixture was incubated in the dark condition for 60 min and the absorbance was recorded at 765 nm using the Infinite 200 PRO microplate reader (Tecan, Switzerland). The total phenol content was expressed in terms of gallic acid equivalents and calculated from the standard curve of gallic acid.

Determination of Procyanidin Content

The procyanidin content in the avocado extract was quantified according to the method described by Kou et al.[43] Briefly, the colorimetric assay was generated by the reaction of p-dimethylamino-cinnamaldehyde (DMACA; 1 mg mL^{-1}) in an ethanol-hydrochloric acid mixture (9:1, v/v) with different concentrations from a standard solution of procyanidin B2. The absorbance was immediately recorded at 640 nm using the Infinite 200 PRO microplate reader (Tecan, Switzerland), and a standard curve was used for subsequent analyses. Samples extracted using acetone/water/acetic acid (70:29.5:0.5, v/v/v) were filtered and allowed to react with DMACA. The absorbance was measured and the total procyanidin content was determined using the following equation:

$$Total\ procyanidin\left(procyanidin\ B2\ equivalent, \frac{mg}{g}\right) = \frac{C \times D \times V}{1000 \times S} \quad (1)$$

Where C is the concentration (mg mL^{-1}) extrapolate from the standard curve, D is the dilution factor, V is the sample extraction volume (mL), and S is sample size (g).

Thin Layer Chromatography (TLC) and Liquid Column Chromatography

The presence of major procyanidins in the powdered extract was initially confirmed by thin-layer chromatography (TLC). Standard solutions (0.2 mg mL^{-1}) of procyanidin B1, procyanidin B2, epicatechin, and catechin were used as references. Aliquots of sample or standards were applied to a 10×5 cm aluminium plate of silica gel 60 stationary phase (F_{254} plates, Merck, Germany), 1 cm from the edge. The plates were air-dried for 5 min before being transferred to the TLC development tank (lined with filter paper, covered with the lid, and pre-saturated with mobile-phase vapour). The plate was allowed to develop with 12 mL of the mobile phase (toluene/acetone/formic acid, 3:6:1) until the ascending

solvent front reached approximately a three-quarter length of the plate. The TLC plates were examined under (a) UV 254 nm and (b) UV 366 nm, before spraying with (c) DPPH (2,2-diphenyl-1-picryl-hydrazyl-hydrate) reagent, (d) ferric chloride reagent, or (e) DMACA reagent. Chromatographs were recorded and visualised using a TLC scanner (CAMAG, Switzerland), and Rf values were calculated. All analyses were performed at 25 °C.

Separation of polyphenols was performed on an Acclaim^{TM} RSLC 120 C18 column (100 mm × 2.1 mm, 2.2 µm) stationary phase using a Thermo Fisher Scientific LC system (Thermo Fisher Scientific Inc., USA) connected to the Bruker Impact II mass spectrometer (Bruker Corp., US) with an electrospray ionization source operated in negative mode (capillary 3000 V, end plate offset 500 V, nebulizer pressure 1.8 bar). Water and acetonitrile with formic acid (0.1% v/v) were used to create a mobile phase with gradient flow rate 1 mL min^{-1}, and acetonitrile was increased from 5% to 100% in 30 min and reduced to 5% for the following 10 min. Spectral scans were recorded with mass to charge ratio between (m/z) 50–1300.

Quality Control of APE

Quality control of APE[44] was performed after freeze-drying, including heavy metal residue analysis, pesticide residue analysis, moisture content analysis, and endotoxin.

Preparation of Nanoparticles

Mesoporous silica nanoparticles (MSN) were synthesized under basic conditions following a previously described protocol.[45] Briefly, 0.1–0.3 g of CTAB was dissolved in 90–100 mL of deionised water and sodium hydroxide (2 M) was added to the mixture under constant stirring. The mixture was allowed to equilibrate for 10–30 min at 70–80 °C. TEOS (0.1–1 mL) was subsequently introduced into the mixture at a rate of 20–50 µL min^{-1} into the mixture under vigorous stirring until the formation of a milky solution was observed. The mixture was stirred at 70–80 °C for another 1–3 h to complete the reaction. The obtained colloidal suspension was then centrifuged to remove unreacted CTAB and the precipitate was collected. The residue was dispersed in 20–40 mL of ethanol/HCl (10:1, v/v) and refluxed at 55–65 °C for 24 h to ensure complete removal of CTAB.[46] The MSN were collected by centrifugation at 12,000 rpm, washed several times with ethanol, and dried at 40 °C for 24 h to obtain a dry powder.

The surface of MSN was modified with amino groups by refluxing nanoparticles with APTES, as described in the reported method with modifications under reflux conditions.[46] In brief, 110–130 mg of MSN was thoroughly dispersed in 35–40mL of absolute ethanol and 200–250 µL of APTES was added. The mixture was then allowed to reflux at 60–70 °C for 24 h under the nitrogen atmosphere. The amino-modified nanoparticles (MSN-NH_2) were collected by centrifugation, washed twice with ethanol, and dried overnight at 40 °C in the vacuum before galactose modification.

Galactose Functionalization

Galactose conjugation on the nanoparticles was performed through a reductive amination reaction.[39] MSN-NH_2, 5–15 mg), together with the desired concentration of galactose, was vigorously dispersed in 1–3 mL borate buffer (pH 9) and allowed to equilibrate under magnetic stirring at 200–400 rpm for 1–3 h. Sodium cyanoborohydride (25 mg) was subsequently added to the mixture, and the reaction was allowed to continue for 16 h at room temperature. Unconjugated galactose was removed by centrifugation, and the final product, GMSN, was collected. The GMSN was dried under vacuum and stored at 4 °C for material characterization (see below), extract loading, and biological evaluation.

Nanoparticle Characterization

Dynamic Light Scattering (DLS)

The average hydrodynamic diameter and polydispersity index (PDI) of the nanoparticles were analysed using a Malvern Nano ZS Zetasizer (Malvern Instruments, UK) with a He-Ne laser at 633 nm at 25 ± 0.5 °C. Nanoparticles were dispersed in deionised water at the concentration of 0.1 mg mL^{-1} and were loaded in polystyrene cuvettes. The measurements were performed in triplicate at a backscattering angle of 173°.

Zeta Potential

The nanoparticle charge and extent of surface modification were analysed using a Malvern Nano ZS Zetasizer (Malvern Instruments, UK). The samples were prepared in DTS 1060 folded capillary cells, and the zeta potential was calculated using software based on the Helmholtz Smoluchowski equation according to the manufacturer.

Transmission Electron Microscopy (TEM)

For morphological evaluation, the diluted samples were deposited on lacy carbon-coated copper grids (EMS, USA) and air-dried overnight. Micrographs were obtained between 5000 and 100,000 times magnification using the JEOL JEM 2010 electron microscope (JEOL Ltd., Japan) operated at 200 kV. The average nanoparticle size was determined from a cluster of 50 nanoparticles using the ImageJ software (version 1.53u).

Brunauer–Emmett–Teller (BET) Surface Area Analysis

Estimation of surface area and pore volume was carried out using nitrogen adsorption-desorption following the Brunauer–Emmett–Teller (BET) method.[47] Samples were first outgassed at 100 °C for 12 h, and isotherms were recorded on the Quantachrome Autosorb-1 analyser (Quantachrome Instruments, US) at −195.65 °C. The pore size distributions were further derived using the Barrett- Joyner- Halenda (BJH) method.[48]

X-Ray Diffraction (XRD)

Material crystallinity was investigated using an X-ray diffractometer (MiniFlex 600, Rigaku, Japan). The diffractograms in the range of 10 to 50° were captured at a scan speed of 2° min^{-1} and 40 kV tube voltage.

Fourier Transform Infrared Spectroscopy (FTIR)

The presence of various chemical groups on the surface of the nanoparticles was determined using an attenuated total reflectance-Fourier transform infrared (ATR-FTIR) spectrometer (Nicolet™ iS5, Thermo Scientific, US). All spectra were collected in the region 4000–400 cm^{-1} with a spectral resolution of 4 cm^{-1}.

Phenol-Sulphuric Acid Test for Galactose Quantification

Galactose attachment to nanoparticle surface was quantified using a phenol-sulfuric acid-based colorimetric assay.[40] Briefly, 2 mL of galactose standard solution (25–200 μg mL^{-1}) was allowed to react with 1 mL phenol (5%, w/v) and 4 mL of concentrated sulphuric acid in sealed glass vials for 15 min. The absorbance was then recorded at 490 nm using the UV 2600 spectrophotometer (Shimadzu, Japan) and the standard curve ($y = 0.0082x + 0.0107$, $R^2 = 0.965$) was obtained. The GMSN (1 mg) was dispersed in 2 mL of water, sonicated for 5 min, and treated as mentioned above to achieve the actual functionalization of the GMSN. Galactose content was calculated from the measured absorbance fitted to the standard equation.

Ninhydrin Test

The extent of galactosylation on the surface of the MSN was further estimated by quantifying the amino groups before and after surface modification using a ninhydrin-based assay.[49] An aliquot of 2 mg of nanoparticle was added to a glass vial and dispersed in 1 mL water. Ninhydrin reagent (2%, w/v; 1 mL) was added to the dispersion, vortexed, and placed in a water bath at 90 °C for 17 min. After the reaction mixture was cooled, 10 mL of water:ethanol (50:50, v/v) was added, and the absorbance was recorded at a wavelength of 570 nm.

pH Sensitivity and Serum Stability

Switching or reversal of the nanoparticle surface charge in response to pH changes was studied in buffered solutions at pH 5.5 and pH 7.4. Nanoparticles were incubated in phosphate-buffered saline (PBS) at pH 7.4 or pH 5.5. An alteration in surface charge density at different pH values was recorded from zeta potential values for 12 h incubation period using a Malvern Nano ZS zetasizer.

The size distribution stability of nanoparticles was studied in vitro, nanoparticles were gently mixed with PBS (pH 7.4) with or without 10% (v/v) FBS and incubated at 37 ± 0.5 °C. Changes in the size and PDI of the GMSN were observed at different time points until 12 h post-incubation. Experiments were performed in triplicate at pH 5.5 to investigate the pH-responsiveness of the nanoparticles.

Extract Loading

Avocado extract was loaded into the nanoparticles following a simple diffusion-filling-precipitation method,[50] and 3–10 mg was dissolved in a PBS: ethanol mixture (1:1 ratio, pH 5.5), and 20 mg of the nanoparticles was added to the extract solution. After an initial sonication for 10 min, the mixture was slowly stirred for 24 h at room temperature (25 °C). The pH of the mixture was re-adjusted to 7 using 0.1 M sodium hydroxide and stirred for another 2 h at room temperature. Extract loaded nanoparticles were harvested by centrifugation, washed with water, and refrigerated (2–8°C) for further use. The supernatant collected after centrifugation was diluted and analysed using a DMACA-based assay (as described in the procyanidin content analysis). The amount of extract loaded was expressed in terms of percentage loading efficiency (%LE) and percentage entrapment efficiency (%EE), calculated using the following equations:

$$\%\,Loading\ efficiency = \frac{weight\ of\ drug\ in\ MSN}{total\ weight\ of\ MSN\ after\ loading} \times 100 \quad (2)$$

$$\%\,Entrapment\ efficiency = \frac{weight\ of\ drug\ in\ MSN}{weight\ of\ drug\ initially\ added} \times 100 \quad (3)$$

In vitro Drug Release

The release of avocado seed extract to the dissolution media at pH 7.4 and pH 5.5 was studied under in vitro sink conditions. Briefly, 2 mg of nanoparticles was dispersed in 1 mL of PBS (containing 20% ethanol, v/v) and was allowed to incubate at 37 ± 0.5 °C in an Eppendorf ThermoMixer C shaker (Eppendorf, Germany) set at 800 rpm. Aliquots of the samples (0.8 mL) were withdrawn at different time intervals through centrifugation and replaced with fresh medium to maintain the sink condition. The samples were appropriately diluted and analysed according to the method described for the procyanidin content analysis.

Cell Lines

A sorafenib-resistant cell line (SR-HepG2) was generated by treating the HepG2 cells with increasing doses of sorafenib tosylate (2.5 μM and 5.0 μM, respectively) adapted from the previous experiment.[51] The cells were incubated with the designated concentration of sorafenib tosylate within high glucose DMEM media supplemented with 10% (v/v) FBS and 1% (v/v) penicillin–streptomycin antibiotics and incubated at 37 °C in 5% CO_2 for 72 h before sub-culturing the viable cells; and this procedure was continued for three rounds per each concentration. Surviving sorafenib-resistant cells were recovered and passaged using the same sorafenib concentration. Once the maximum concentration of sorafenib is used to produce resistant cells; the 5.0 μM concentration will be included as "SR5.0-HepG2" to represent the resistant cells.

Cellular Uptake and Distribution

Cell Uptake Kinetics

The internalisation of nanoparticles in the two different cell types and their ability to escape from endosomes were evaluated in a 96 well-plate (PhenoPlate, Perkin Elmer, US) on a high-content imaging platform (Opera Phenix® Plus, PerkinElmer, Germany). The fluorescein isothiocyanate (FITC) tagged nanoparticles (FI-MSN-NH_2 and FI-GMSN) were prepared by incubating 10 mg of the nanoparticles overnight in ethanol containing 2 mg FITC. The nanoparticles were recovered by centrifugation at 14,000 rpm and stored at 2-8°C until further use. For real-time cellular uptake and distribution analysis, the nanoparticles were redispersed in serum-free DMEM (50 μg mL^{-1}, 200 μL) and incubated for 2, 4, 8, and 24 h. Cells were washed with DPBS to remove all unbound nanoparticles and subsequently stained for 10 min with Hoechst 33342 (1 μg mL^{-1} Invitrogen, Thermo Fisher Scientific, US) and wheat germ agglutinin (1 μg mL^{-1} WGA,

Thermo Fisher Scientific, US) to visualise the nuclei and cell membranes, respectively. The intracellular distribution of the nanoparticles was observed using a 40×1.1 N.A. water immersion objective by Opera Phenix® Plus high content imaging system (Perkin Elmer, Germany) maintained at 5% CO_2 and 37 ± 0.5 °C. The background was checked according to the thickness of the stack images and parameters, including stack size, the laser power, and exposure time, were kept constant for all samples, although the spinning disk technology provides improved image quality and reduces interferences between fluorescence channels.[51] Confocal images at 2160×2160 pixels obtained from 16 random fields with 4 µm thick section were analysed using Harmony software (version 5.1). Cells were identified using "Find cell" building block and the nanoparticles trafficked inside the cells were marked using the "Find spots" function. The total nanoparticles inside the cells (mean fluorescence intensity (MFI)) at different time intervals were plotted.

Endosomal Escape Capacity

For the endosomal escape study,[52,53] non-fluorescent nanoparticle dispersions (50 µg mL^{-1}, 200 µL) were used. At the end of each incubation period, the cells were washed and stained with acridine orange AO (Santa Cruz Biotechnology, USA) in DMEM (5 µg mL^{-1}) for 10 min. The distribution of endosomes across the cells was observed, and confocal images obtained from 16 random fields with z-stacks of 4 µm thick section were analysed using Harmony software. The background was checked according to the thickness of the stack images, and parameters including stack size, laser power, and exposure time were kept constant for all samples. The MFI of the endosomes (red fluorescent signal) and cytosol (green fluorescent signal) was identified and quantified using Harmony software. The number of endosomes present within the cytosol was calculated using an image analysis pipeline and the data were plotted with respect to time.

Anticancer Activity Studies

WST-1 Assay

The cytotoxicity of crude APE and its nano-encapsulated forms was evaluated in HepG2, SR5.0-HepG2, and Huh-7 cell lines. Briefly, 3×10^4 cells were seeded in 96-well plates. Cells were allowed to reach 70% confluence and were then treated with different concentrations (20–100 µg mL^{-1}) of APE, MSN-NH_2@APE, and GMSN@APE dispersed in serum-free DMEM. All the nanoparticles were ultrasonicated for 2 min at room temperature before the treatment. The cells were incubated with nanoparticles for 24 h, and the treatment media was replaced with 100 µL of WST-1 (Roche, Germany)-containing media (5%, v/v). The plates were further incubated for 15 min, and absorbance was measured at 440 nm using the Infinite 200 PRO microplate reader (Tecan, Switzerland). Cell viability was calculated as the percentage of cell viability compared to the control non-treated cells.

LDH Assay

The extent of cell membrane damage caused by APE and nano-encapsulated forms at their IC_{50} concentrations was evaluated using the LDH assay for a 24 h exposure period (Roche, Germany) according to the manufacturer's instructions. Briefly, 50 µL of cell-free medium from each group was mixed with 50 µL of freshly prepared LDH mixture (containing the LDH substrate and assay buffer) in a 96 well plate. Cells without treatment were considered as the control group, and cells lysed with Triton X-100 were used as the positive control to indicate the total LDH concentration in the cells. Additional controls consisting of empty MSN-NH_2 and GMSN dispersed in serum-free DMEM were used to confirm the non-interference of the nanoparticles with the assay reagent. The plate was incubated in the dark for 30 min, and the absorbance was recorded at 490 nm.

Statistical Analysis

All experiments were performed in triplicate (n = 3), and the data are expressed as mean ± standard deviation (SD). One-way ANOVA followed by Tukey's post hoc test was performed for surface charge comparisons and cytotoxicity data using GraphPad Prism 8.0.1. Observations were considered to be significant with the confidential interval of *$p<0.05$, **$p<0.01$, and ***$p<0.001$.

Results and Discussion

Quality Control and Characterization of APE

Avocado seeds are known to contain a variety of bioactive compounds such as polyphenols, flavonoids, procyanidins, and fatty acids.[14] Their chemical profile is strongly influenced by its origin, season, variety, post-harvest, and cultivation conditions.[54] An orange-coloured powder was extracted from the avocado seeds through simple maceration with a yield value of 14.53% (w/w) and contained antioxidants, polyphenols and procyanidins, as procyanidin B1, procyanidin B2, epicatechin and catechin were evidently observed in thin-layer chromatograms (Supplementary Figure 1). The colour of the lyophilized extract is associated with a constituting glycosylated benzotropone compound called "perseorangin".[55] Water and ethanol have advantages over other extraction solvents, including versality, safety and economically.[56] Detailed quantification through colorimetric assays confirmed total phenolic contents of 73.81 ± 2.34 mg per gram, and total procyanidin content of 655.35 ± 44.54 mg per gram of the powder, using gallic acid ($y = 0.0069 + 0.1077$, $R^2 = 0.9978$) and procyanidin B2 ($y = 0.0037x + 0.0379$, $R^2 = 0.9995$) as respective standards. Phytochemical profiling of APE by LC-MS also revealed the presence of gallic acid and catechin-gallic acid derivatives (Supplementary Figure 2 and Supplementary Table 1). These polyphenols are well-known anticancer agents with profound proapoptotic activity under experimental conditions.[57,58] All impurity residues in APE met the requirements of the Thai Herbal Pharmacopoeia 2020.[44] The presences of arsenic, cadmium, lead and mercury were not detected at detection limits of 0.010, 0.01, 0.01, and 0.007 ppm, respectively. Pesticide residues were not detected in APE. Moisture content is an important factor in determining the stability of powder storage. The percentage of the moisture content of APE was 8.09 ± 0.14% which aligns with the recommendation of Thai Herbal Pharmacopoeia 2020,[44] where the herbal product should contain less than 10% of moisture content to prevent product instability and microbial contamination. The endotoxin level was found to be between 0.0647 and 0.0915 EU/mL, indicating the low endotoxin levels in APE.

Nanoparticle Design and Characterization

MSN were obtained under hot alkaline conditions, and the cationic surfactant CTAB was used as a template for micelle formation with subsequent condensation of high-density silicates around the preformed micelles due to strong electrostatic interactions.[59] Post-synthesis amino grafting was preferred for co-condensation, since we intended to modify only the exposed outer silanol groups, leaving the inner pore chemistry intact for easy drug diffusion.[60] Galactose conjugation was carried out via reductive amination using sodium cyanoborohydride as the reducing agent.

The TEM images revealed that the nanoparticles were monodisperse and uniform spheres (Figure 1A, C, E). TEM images at higher magnifications (Figure 1B, D, F) showed the obtained nanoparticles possessed typical size (MSN: 127.25 ± 31.12 nm, MSN-NH_2: 115.56 ± 12.86 nm, GMSN: 125.41 ± 10.91 nm (n = 50)) with an open-ended lamellar-type arrangement of hexagonal pore tubules (inset Figure 1B). Mesoporous structures are clearly observed (see Figure 1B, D, and F). Amination of the outer silanols (Figure 1D) and further galactosylation (Figure 1F) did not significantly affect nanoparticle morphology. Dynamic light scattering records showed a mono-size distribution of MSN particles (PDI: 0.324 ±0.02) with an average hydrodynamic diameter of 237.6 ±11.93 nm (Figure 1G). Being similar in morphology between MSN and MSN-NH_2, the GMSN, however, demonstrated a slight decrease in PDI to 0.256 ± 0.022 (average hydrodynamic diameter 224.6 ± 2.46 nm, n = 3), probably due to the presence of a hydrophilic layer of galactose molecules that appeared transparent to electron microscope (Figure 1F).[40] This hydrophilic layer also seemingly contributed towards improved dispersibility of the GMSN in aqueous medium through the lowering of nanoparticle surface energy. In fact, the coating of the surface with various mono- and oligosaccharides has been a routine strategy to maintain nanoparticle dispersity especially during storage.[61] Zeta potential measurements (Figure 1H) revealed that amino surface modification caused charge alteration from −27.3 ± 4.25 mV to +18.5 ± 0.40 mV, probably due to the conversion of the surface silanol groups to positively charged amino groups. Water-dispersed GMSN carried negative surface charges (−18.2 ± 0.32 mV, n = 3) signifying galactose surface-conjugation. The variation in the ratio between galactose and nanoparticles (Supplementary Table 2) demonstrated that a high ratio of galactose significantly increased the hydrodynamic diameter of the final nanoparticles, along with a proportionate increase in the zeta potential at pH 7.4. The ratio of galactose: nanoparticles used in the reaction as well as the reaction time (Supplementary Figure 3) are two critical factors that influence the size and surface charge of the final GMSN. Thus,

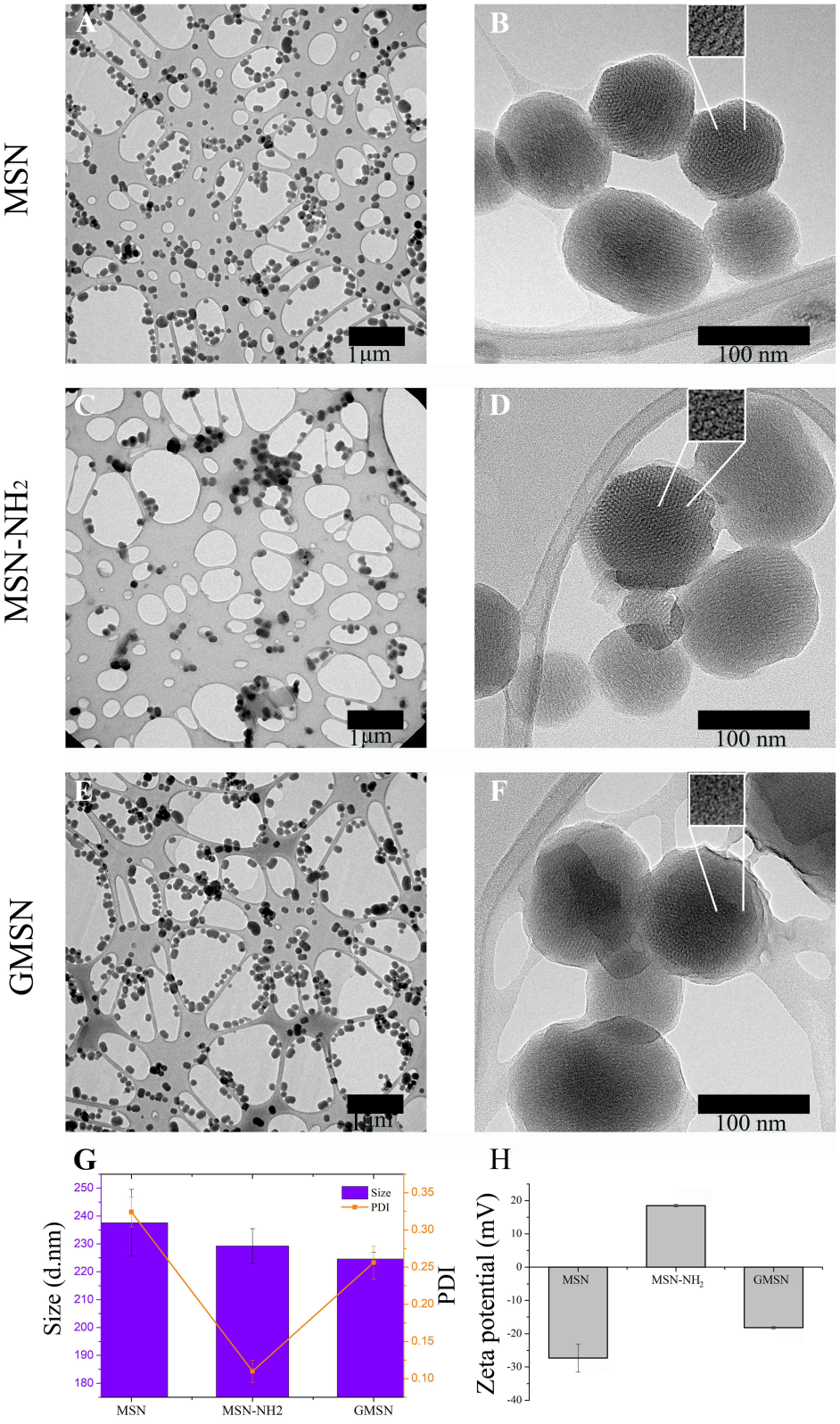

Figure 1 Nanoparticle characterization, transmission electron micrographs (**A**–**F**), size distribution and surface charge density of MSN (**A** and **B**), MSN-NH_2 (**C** and **D**) and GMSN (**E** and **F**). Scale bars are 1 μm in (**A, C, E**), and 100 nm in (**B, D, F**). Insets in (**B, D**, and (**F**) show the mesoporous surface of individual nanoparticles. Data of particle size and surface in (**G** and **H**) are expressed as mean ± SD, n = 3.

to restrict the particle size and create a pH-responsive capacity, a ratio of 1:2 (galactose: nanoparticles) was fixed for 16 h of reaction time.

The CTAB residuals can affect the cellular toxicity of nanoparticles. Compared to the CTAB, the complete extraction of CTAB templates was confirmed by FTIR results (Figure 2A), showing the absence of characteristic peaks at 2916, 2844, and 1470 cm^{-1} in all MSN panels.[62] The FTIR analysis also demonstrated in Figure 2A that the inherent silanol peaks at 964 cm^{-1} (dashed line blue arrow) were markedly diminished after amino grafting in MSN-NH_2 and MSN-NH_2@APE. Another major band between 3500 cm^{-1} and 3000 cm^{-1} arising from the Si-OH group in the MSN, was absent in the case of MSN-NH_2 (dashed blue arrows). However, new absorption peaks were observed in the MSN-NH_2. The small peaks at 1560 cm^{-1} and 3460 cm^{-1} represented the N-H stretching and C-H bending of the primary amine, respectively, signifying successful chemical conjugation on the silica surface.[63] In the case of galactose functionalization (GMSN), the mechanism of covalent bond formation between the aldehyde group of galactose in the ring-open state and exposed amino-propyl groups on the nanoparticles was previously described by Nartowski et al[64] and was evident from the vibrational peaks at 1470 cm^{-1} and 1410 cm^{-1} (green arrows). The FTIR data also confirmed the presence of APE in MSN-NH_2 and GMSN (Figure 2A). Characteristic peaks between 3500–3000 cm^{-1}, 2929 cm^{-1} and 1620 cm^{-1} (purple arrows) represent the O-H, C-H, and C=C stretching of aromatic compounds in the extract. These peaks were profound in the spectra of the loaded nanoparticles. Extract loaded nanoparticles also featured minor absorption bands at 1387 cm^{-1} arising from methylene groups and at 960 cm^{-1} (purple arrows) arising from C-O vibrations, signifying polyphenolic contents.[65] One shoulder peak at 1711 cm^{-1} present in the spectrum of pure APE due to C=O stretching appeared in lower intensity for GMSN@APE and MNS-NH_2@APE nanoparticles.[66] It is likely that phytochemicals with carbonyl groups can extend non-covalent interactions with nanoparticle surface amino-groups during their encapsulation. This interpretation is further supported by the disappearance of the characteristic amino peak (1560 cm^{-1}) originally present in the MSN-NH_2 spectrum, as observed in the GMSN@APE and MNS-NH_2@APE nanoparticles (Figure 2A). The amorphous nature of MSN was revealed by the broad XRD peak between 20° and 30° (Figure 2B) and was consistent with earlier studies.[67,68] Although the change in crystallinity upon amine modification was insignificant, galactose functionalization caused a shift in the diffraction maxima to 21° (see arrow in Figure 2B). This indicates a slight change in the lattice structure. Galactose functionalization of other nanoparticle types, such as PLGA, chitosan, and layered double hydroxide, has similar distortive effects on material crystallinity and presents opportunities for uniform degradation.[69–71] It must be mentioned here that while the crystalline nature of the crude extract was evident from the strong diffraction peaks between 15° and 30°, nanoparticle loading via the diffusion-filling-precipitating technique could cause the extract to lose its crystallinity and exist in an amorphous state inside the silica mesopores (Figure 2B). The galactose content determined through the phenol-sulfuric acid-based colorimetric assay was found to be 33.46 ± 2.42 µg per mg of nanoparticles, indicating efficient galactose molecular installation on the nanoparticle surface. The results from colorimetric quantified amino groups using ninhydrin-based reactions confirmed that approximately 55% of the original amino groups were galactosylated on the GMSN surface.

The surface area and pore structure of the nanoparticles were further analysed using nitrogen adsorption-desorption isotherms. The type IV isotherm, according to the International Union of Pure and Applied Chemistry,[72] was identified from the presence of an H1 hysteresis loop (Figure 3A, C, and E) and confirmed the mesoporous nature of the nanomaterial.[73] The onset of reversible capillary condensation at a relative pressure (P/P_o) of 0.2–0.32 was due to the hexagonal pore arrangement,[74] as revealed by the TEM micrographic images in Figure 1B, D, and F. Furthermore, the near-parallel branches of the nitrogen adsorption-desorption branches indicated a narrow pore size distribution.[75] The BET surface area and pore volume of the MSN were found to be 526.43 $m^2\ g^{-1}$ and, 0.41 $cm^3\ g^{-1}$ respectively (Figure 3A and B). The pore size, as derived through the BJH method,[48] was about 3.13 nm. In the case of MSN-NH_2, the BET surface area and pore size were 667.60 $m^2\ g^{-1}$ and 4.2 nm, respectively (Figure 3C and D). The surface area of the GMSN was considerably reduced to 185.11 $m^2\ g^{-1}$, though the pore size was calculated to be 2.01 nm (Figure 3E and F). This data indicate that galactose molecules were mostly conjugated to the nanoparticle outer surface rather than perturbing the inner pore chemistry.

Nanoparticle Stability and pH-Dependent Charge Switch

During the transition from the physiological environment to the acidic tumour microenvironment, nanoparticles should feature the positive charge to facilitate internalisation by tumour cells via endocytosis. Therefore, pH-responsiveness and surface charge-switch capacity were evaluated by incubating the nanoparticles with a buffer at pH 7.4 and pH 5.5. The

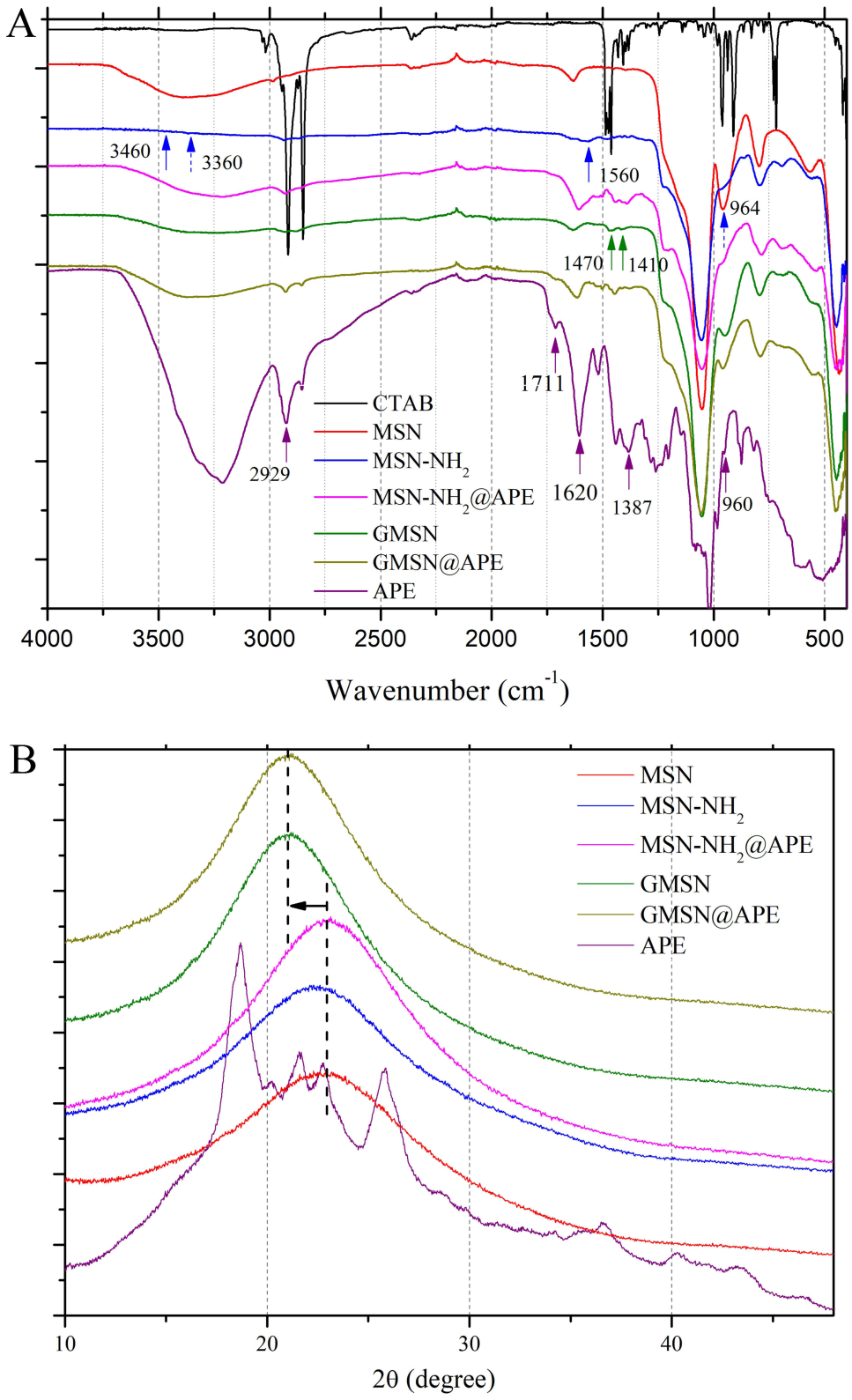

Figure 2 Chemical characterization of nanoparticles using FTIR (**A**) and XRD (**B**): (**A**) FT IR spectra of MSN, MSN-NH_2, GMSN, APE loaded nanoparticles, MSN-NH_2 @APE, GMSN@APE, in comparison to CTAB and APE. (**B**) XRD spectra of MSN, MSN-NH_2, GMSN, APE and APE loaded nanoparticles.

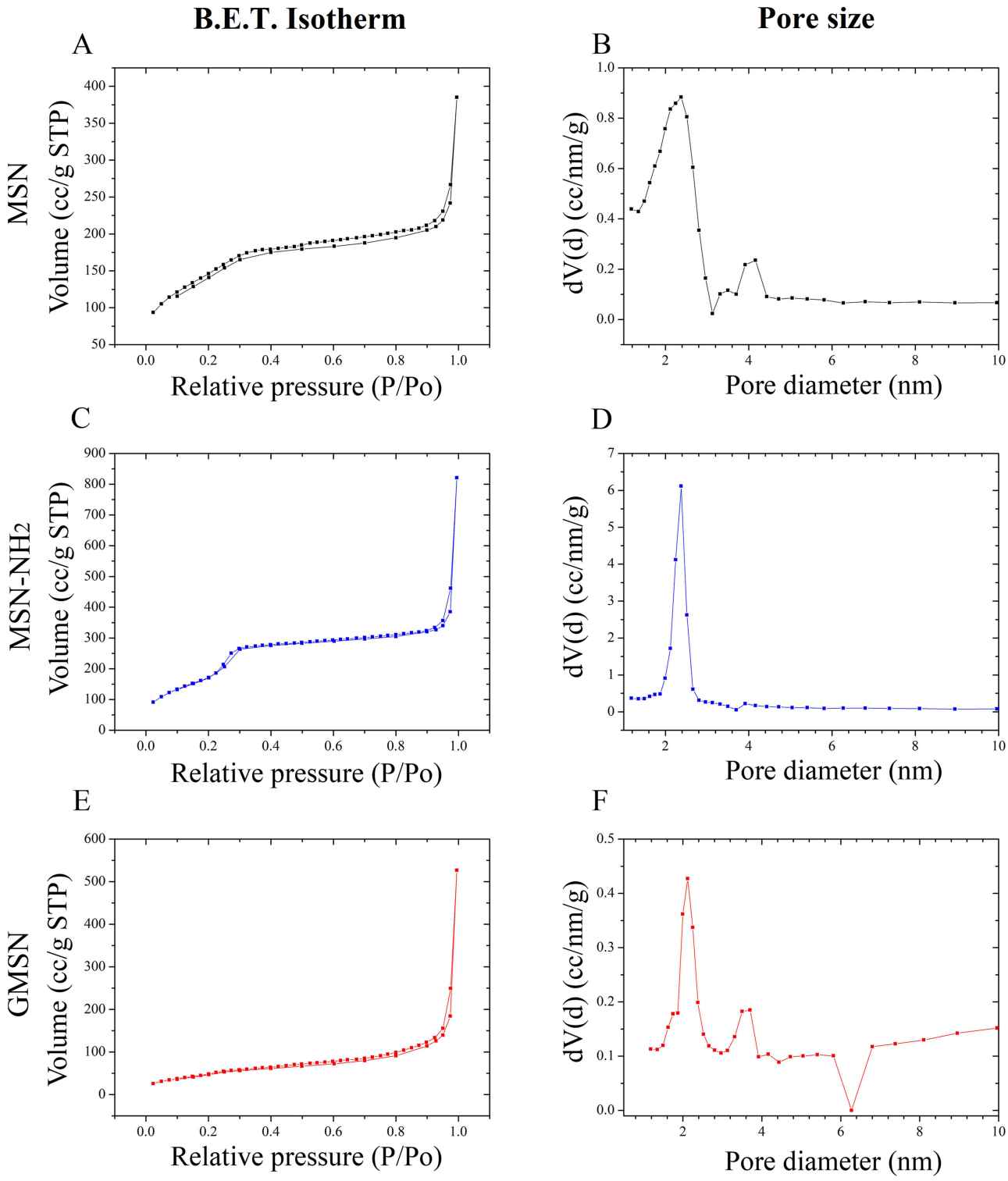

Figure 3 Nitrogen adsorption-desorption isotherm and pore size distribution of MSN (**A** and **B**), MSN-NH_2(**C** and **D**), and GMSN (**E** and **F**).

surface of galactose modified nanoparticles showed a negative charge (−18.2 ± 0.32 mV, n = 3) upon dispersion in medium of pH 7.4 (Figure 4A). This is due to the exposed hydroxyl groups of anionic galactose molecules with a pKa value of ~13, which is consistent with other reports on galactose-conjugated nanoparticles.[33,76] Additionally, at neutral pH, the amino groups remained unionised and did not affect the surface charge density. However, at pH 5.5, positive

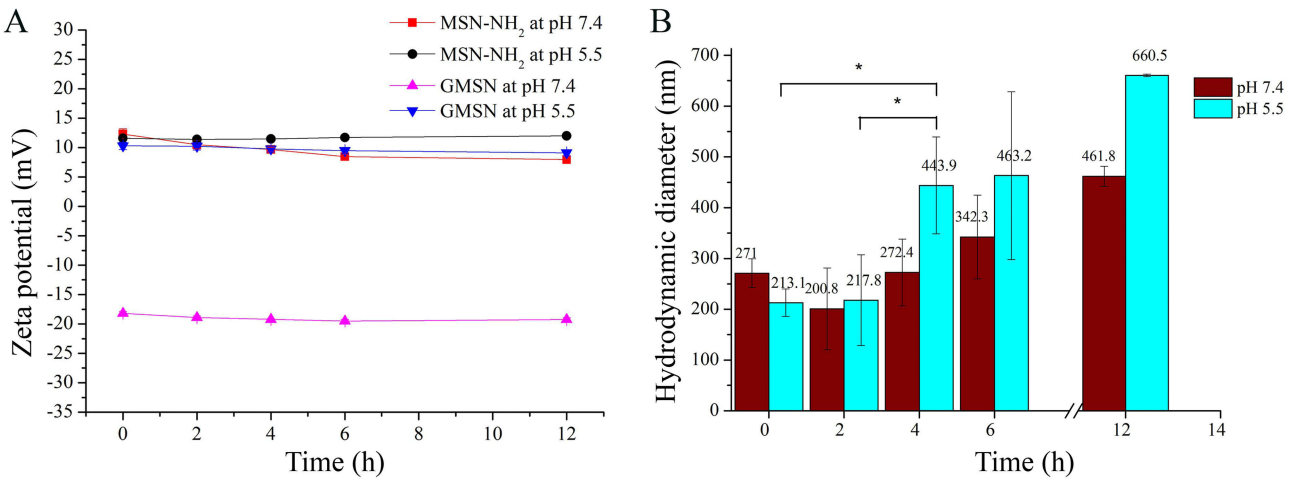

Figure 4 Effect of serum on size and surface charge of MSN-NH_2 and GMSNs: (**A**) Nanoparticle surface charge at pH 7.4 and pH 5.5. (**B**) Nanoparticle particle size in 10% FBS containing media at pH 7.4 and pH 5.5. Data expressed as mean ± SD (n = 3); the significant difference was reported at *p < 0.05.

charges were predominant on the nanoparticles (10.3 ± 0.61 mV, n = 3). As the pKa value of the amino groups in the original APTES molecules is 10, they are likely to be ionised and protonated ($NH_2 + H^+ \rightarrow NH_3^+$) in an acidic environment, thus contributing to the positive charge on the GMSN surface. Our preliminary trials (Supplementary Table 2) demonstrated that nanoparticles surface-conjugated with higher amounts of galactose did not exhibit a significant positive charge at acidic pH, possibly because of the consumption of amino groups during galactose attachment. Therefore, selective galactosylation (approximately 55%) can cause charge alterations on nanoparticle surfaces, that is based on the protonation of unmodified amino groups and deprotonation of hydroxyl groups of galactose at different pHs. Unmodified MSN-NH_2 was used as a control, as it demonstrated positive zeta potentials under both acidic and neutral conditions owing to the presence of surplus amino groups.

Once nanoparticles enter the systemic circulation (pH 7.4), they extend non-specific interactions with proteins in their immediate vicinity, thus initiating a dynamic process of association-dissociation of proteins on their surface. The interactions between proteins and nanoparticles are usually governed by multiple parameters such as nanoparticle size, shape, and surface chemistry.[77] Usually, cationic nanoparticles prefer to aggregate through non-specific interactions with the blood components. Conversely, anionic nanoparticles tend to retain their stability in physiological environments and display enhanced ability to overcome systemic barriers.[78] At physiological pH (pH 7.4), galactose functionalized nanoparticles demonstrated a certain degree of stability and no significant difference in hydrodynamic diameter ($p > 0.05$) for 6 hours of incubation period with 10% serum media (Figure 4B). At pH 5.5, nanoparticle aggregation was more prevalent during the first 4 h of incubation. A significant increase in hydrodynamic diameter of the nanoparticles from 213.1 ± 27.11 nm to 443.96 ± 95.4 nm within 4 h could be explained by the protonation of amino groups and consequently switching to cationic charges at acidic pH, thereby increasing the chances of protein deposition. Cationic nanoparticles may[79,80] or may not[81] mediate protein destabilisation. However, the strong interactions with amino acid residues may lead to the precipitation of proteins on the nanoparticle surface.[79,80] Our nanoparticle design highlights formulation stability in physiological environments and presumably can retain original surface functionalities for extended periods of time. This is essential for the subsequent targeting of cancer cells under clinical conditions.

Drug Loading and Release in vitro

The encapsulation of plant extracts is affected by mesoporous surface chemistry as well as by the pH of the loading medium. It is well known that acidic pH (pH 5.5) favours protonation of the exposed amine groups on the nanoparticle surface,[38] that extends the interactions with negatively charged avocado extracts (−32.6 ± 1.14 mV). Zeta observations demonstrated that pH-restoration to 7.4 caused deprotonation of the amino groups. Therefore, we hypothesized that the diffusion-filling-precipitation method (Figure 5) would support the maximum quantity of extract loading in the

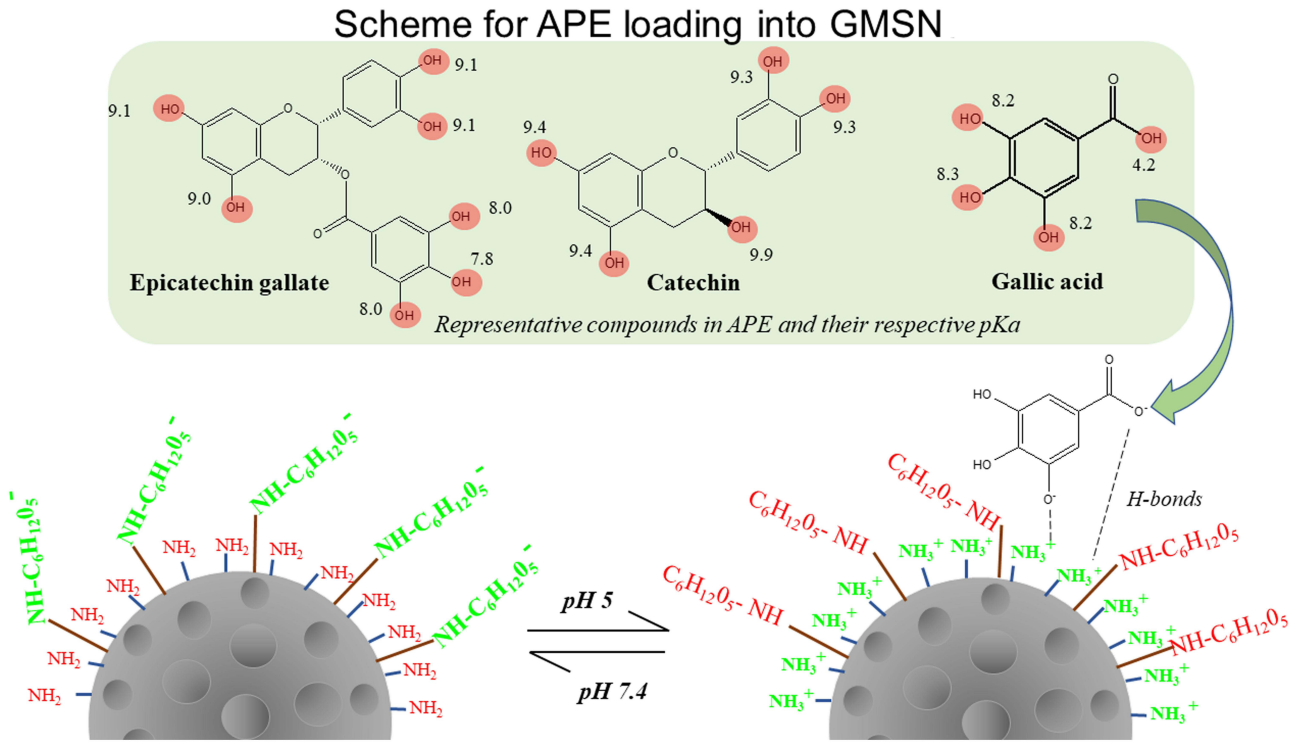

Figure 5 Loading mechanism of APE into galactose-modified mesoporous structures (GMSN) through diffusion-filling-precipitation. Interaction between ionizable groups of avocado seed extract constituents and cationic amino-groups at acidic pH.

mesoporous structure. Once loading into the mesopores was achieved, the pH of the loading medium was changed to neutral (pH 7) to prevent the leakage of the extracts from the loaded nanoparticles. This cargo loading mechanism is simple and can be applied to new-generation pH-responsive nanocarriers. APE loading into the MSN-NH_2 and GMSN did not significantly affect the nanoparticle size (MSN-NH_2:126.31 ± 19.21 nm, GMSN: 131.41 ± 14.41 nm (n = 50)), although zeta potential variation for both APE@MSN-NH_2 (+13.68 ± 0.74 mV) and APE@GMSN (−35.4 ± 1.35 mV) confirmed the presence of cargo on the nanoparticle surface. Earlier studies on diffusion-filling-precipitation techniques were restricted to doxorubicin loading into mesoporous silica nanoparticles and have not yet been tested for the encapsulation of plant extracts or any other bioactive molecules.[82,83]

Different ratios between the extract mass and carrier mass, and different loading periods were evaluated to finally optimise the encapsulation protocol and achieve the highest loading percentages (%LE) and entrapment efficiencies (% EE), as shown in Supplementary Figure 4. The MSN-NH_2 had a drug loading of 52.88 ± 3.64% and entrapment efficiency of 50.86 ± 2.23% (Figure 6A). The GMSN, however, showed inferior loading capacity and entrapment efficiency of 41.08 ± 2.09% and 44.96 ± 2.26%, respectively. Galactose functionalization leads to a relative scarcity of protonated amino groups on the GMSN surface which usually promotes the loading process at acidic pH.

The encapsulated drug in nanocarriers is ideally designed to prevent premature leakage of precious bioactive cargo and avoid side effects on normal tissues. In vitro dissolution studies revealed a pH-dependent sustained release of avocado extract from the nanoparticles, favouring an acidic pH (pH 5.5) rather than a physiological pH (pH 7.4). A burst release phenomenon was evident within the first 2 h (Figure 6B), which occurred because of the release of the loose cargo adsorbed on the surfaces.[68] In fact, a major part of the extract entrapped by the GMSN was adsorbed on the surface, thus offering a burst release of ~45% at pH 5.5 which is almost twice as much as from the MSN-NH_2 nanoparticles (*$p < 0.05$). Protonation of the surface amino groups at acidic pH also promoted the release of the extract from the mesopores.[84] On the other hand, the release of cargo at physiological pH appeared less (**$p < 0.01$) due to deprotonation of the surface galactose. This phenomenon was more evident (cumulative release <25%) when MSN-NH_2 nanoparticles were dispersed in pH 7.4 medium. This pH-dependent release behaviour is one of the necessary features in

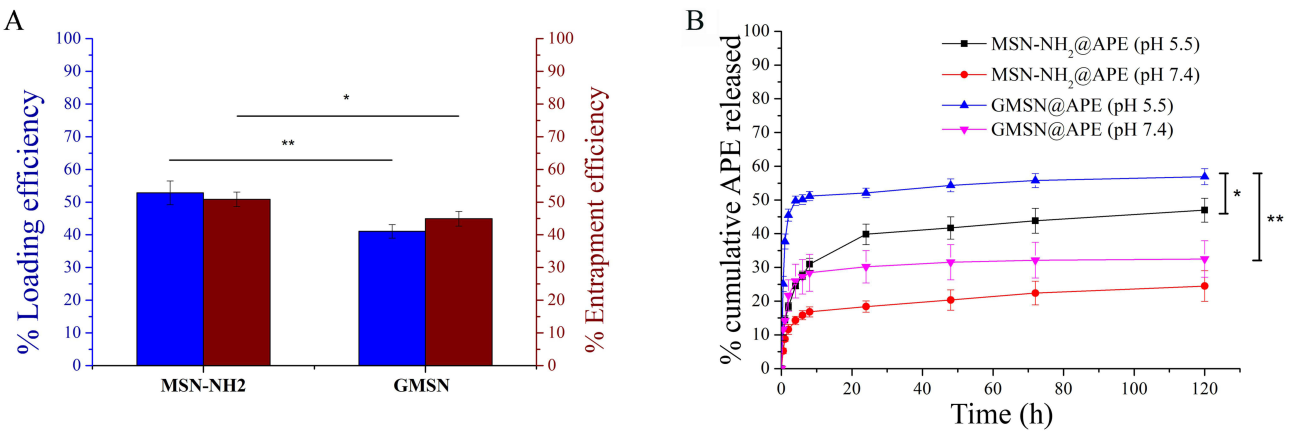

Figure 6 Percentage of drug entrapment efficiency (%EE), loading efficiency (%LE) and the release of APE loaded MSN-based nanoparticles: (**A**) Drug loading and entrapment efficiency of MSN-NH_2 and GMSN. (**B**) In vitro release of APE at pH 7.4 and pH 5.5. Data expressed as mean ± SD (n = 3, *p < 0.05, **p < 0.01).

the design of cancer -cell targeted nanoparticle design. The mesoporous structure of nanoparticles also played its part in the cargo release mechanism. As opposed to others nanocarriers, such as biopolymers and solid lipids, mesoporous silica offers a higher surface area which is an important factor for cargo adsorption as well as for the burst release velocity.[85] The release of the extract gradually reaches a maximum over 8 h in both acidic and physiological pH and follows a steady state mass transfer thereafter.

Targeting Efficiency and Endosomal Escape

Galactose and its derivatives have been established as targeting ligands for the delivery of nanoparticles into HCC cells in several works.[34,70,71,86,87] The FITC labelled GMSN (FI-GMSN) was used for cellular distribution studies in comparison to the non-targeted particles, FI-MSN-NH_2 (Supplementary Figure 5). The Harmony® software (Supplementary Table 3) allowed quantification of FI-GMSN in the intracellular regions of interest (ROIs) in specific cell organelles. HepG2 cells were reported to express ASGPR at a density of 76,000 receptors/cell.[88] Images obtained from the HepG2 and SR5.0-HepG2 cell lines at 2 h of incubation (Figure 7A and B) revealed that the FI-MSN-NH_2 nanoparticles are attached on the cell membranes but only very few were completely internalized by the cells over 24 h. The FI-GMSN, however, showed early signs of internalization at 2 h, followed by saturation within 24 h (Figure 7A). Image analysis quantified and compared to FI-MSN-NH_2 showed that the uptake of the FI-GMSN at 24 h was higher by 3.4 folds in both HepG2 (Figure 7C and D) and SR5.0-HepG2 cell lines, respectively (Figure 7E and F). Comparing between HepG2 and SR-HepG2 cells (Supplementary Figure 6), our results (Figure 7D, F) indicated a similar uptake kinetic suggesting that galactose surface functionalization continued to encourage nanoparticle uptake, although HepG2 cells developed resistance to sorafenib. It was well established in other studies that ASGP receptors retain their expression during the development of sorafenib resistance.[89] Thus, galactose surface-modified, pH-switchable nanoparticles can be exploited for the targeted delivery of anticancer agents to sorafenib-resistant HCC cells.

While galactose surface molecules ensure the selective uptake of nanoparticles into cancer cells via endocytosis, most nanocarriers entering through this pathway are typically sequestered into acidic lysosomes. Thus, endosomal escape has been considered as another "bottle-neck" for on-demand intracellular delivery and gene therapy.[90,91] Although there is an ongoing debate regarding the efficacy of various endocytosis escape assays (such as fluorescence correlation spectroscopy, NanoClick and split green fluorescence protein),[92] we adopted the standard AO stain in tandem with high content imaging modality (Supplementary Table 4) to observe the presence and disruption of late endosomes over time. AO is a cell-permeant nucleic acid-binding dye that produces red fluorescence in the acidic environment of lysosomes, but emits green fluorescence upon leakage into the cytosolic compartment.[93] Both the MSN-NH_2 and GMSN were able to disrupt the endosomes in normal HepG2 cells gradually from the beginning until the end of the treatment phase (0 to 24 h, Figure 8A and B). It can be hypothesised that, owing to the presence of surface amines, the nanoparticles are protonated inside the acidic endosomes and

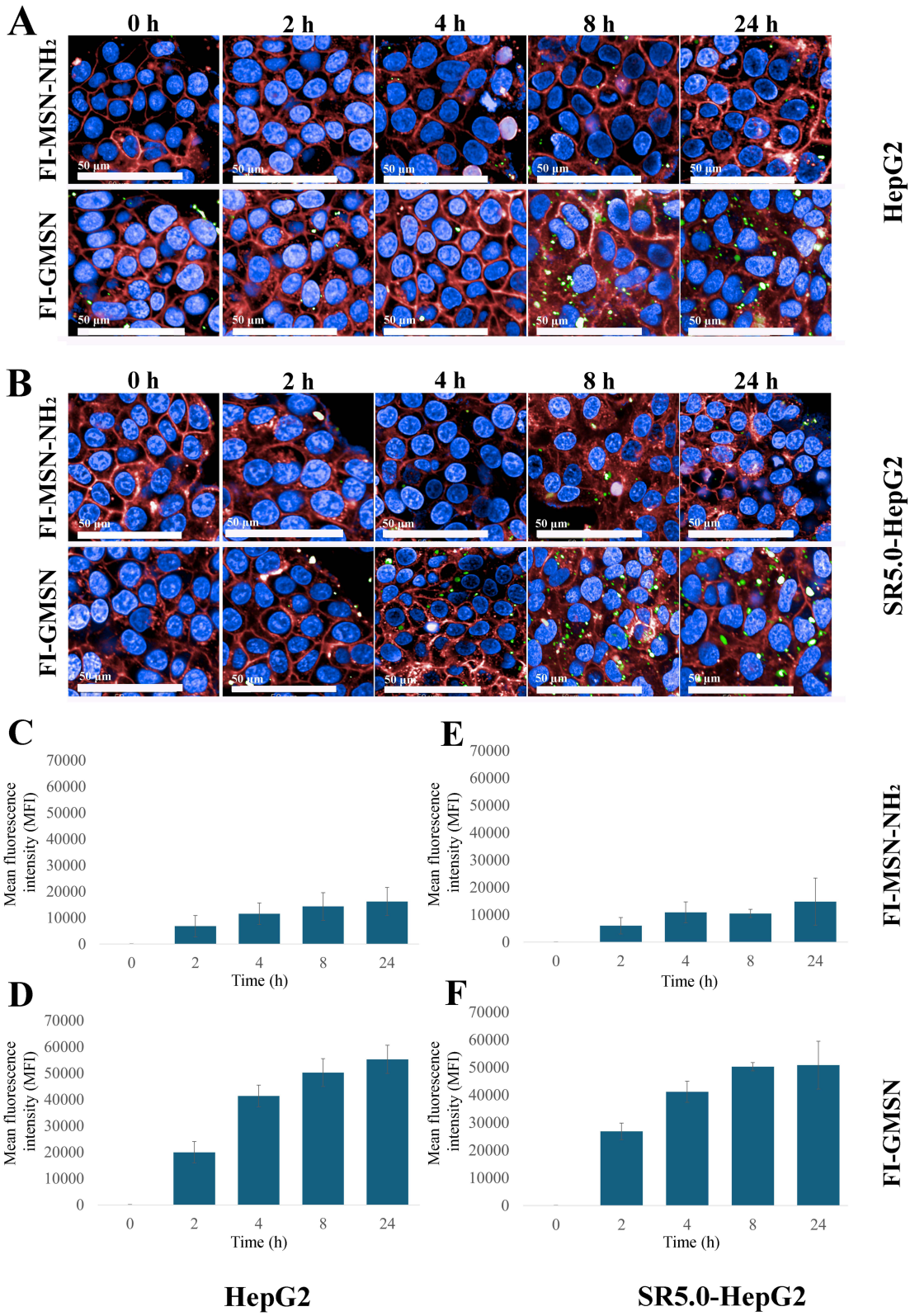

Figure 7 Cellular distribution of FI-MSN-NH_2 and FI-GMSN in HepG2 (**A**) and SR5.0-HepG2 cells (**B**) at 0, 2, 4, 8, 24 h. Cells were exposed to FITC tagged nanoparticles (50 µg mL^{-1}) and visualised using high content imaging in real-time. Nuclei were stained with Hoechst 33342 (blue), cell membranes were stained with WGA (red) and FITC tagged nanoparticles, FI-GMSN and FI-MSN-NH_2 appeared green. Scale bars are 50 µm. Quantification of uptake of FI-MSN-NH_2 and FI-GMSN by (**C** and **D**) HepG2, and (**E** and **F**) SR5.0-HepG2 cells. Data were expressed as mean ± SD (n = 3).

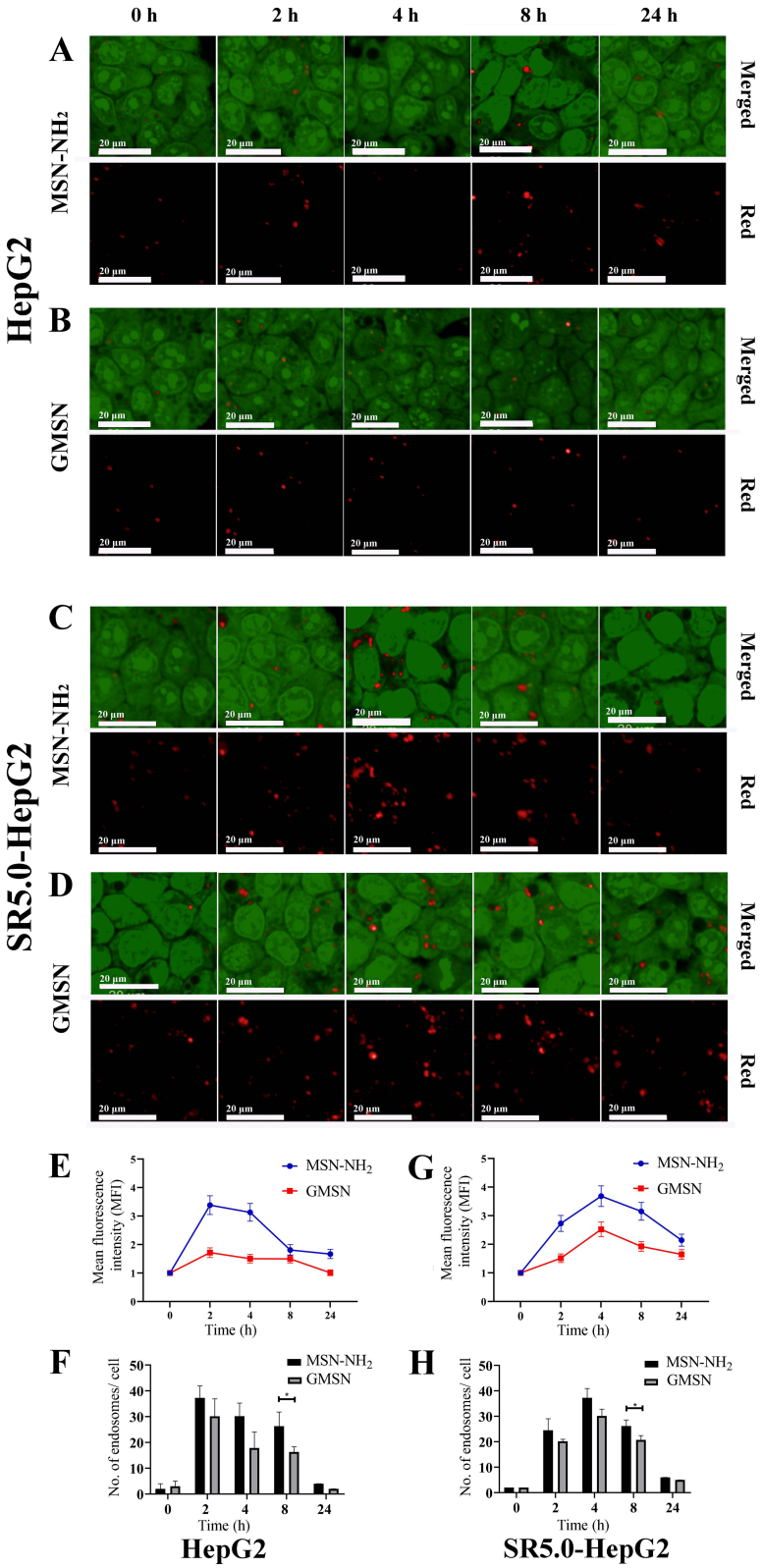

Figure 8 Endosomal escape ability of the MSN-NH_2 and GMSN in (**A** and **B**) HepG2 and (**C** and **D**) SR5.0-HepG2 cells. Maximum projection images are generated from confocal stack images, 4 μm thick, showing the distribution of endosomal vesicles (red) within the cytosol (green) at 0, 2, 4, 8 and 24 h. Scale bars are 20 μm. Quantitative analysis of endosomal escape by MSN-NH_2 and GMSN in (**E** and **F**) HepG2, and (**G** and **H**) SR5.0-HepG2 cells. Fluorescent read-outs (**E, G**) were used to quantify the number of endosomes per cell (**F, H**) at different time points. Data were expressed as mean ± SD (n = 3); the significant difference was reported at *p < 0.05.

cause an influx of protons, counterions, and water molecules to counteract the buffered pH change. This "proton sponge" phenomenon ultimately leads to vesicular disruption due to an osmotic imbalance.[94] It is obvious that MSN-NH_2 have a higher tendency to protonate and internalise inside the endosomes within 2 h, and their endosomal escape ability is slightly better than the galactose modified nanoparticles (Figure 8E and F). However, the presence of endosomes in SR5.0-HepG2 cells appeared prominent until 4 h of nanoparticle treatment (Figure 8G and H). Thereafter, leakage of endosomes occurred after 8 h, signifying the escape of nanoparticles into the cytosol via vesicular disruption. Development of resistance in cancer cells is often associated with lysosomal malfunction, that probably increased sequestering of the nanoparticles in SR5.0-HepG2 cells.[95] Disruption of the endosomal membrane and lysosomal distribution within cells returned to normal due to the successful escape of nanoparticles from the endosomes within 8 h of treatment.

Anticancer Activity of MSN-NH_2, GMSN and GMSN@APE on Non-Resistant and Resistant HepG2 Cells

Both free APE and APE-loaded nanoparticles (MSN-NH_2@APE and GMSN@APE) demonstrated a dose-dependent chemotherapeutic effect in non-resistant HepG2 cells (Figure 9A), whereas non-loaded nanoparticles (MSN-NH_2 and GMSN) demonstrated no cytotoxicity. However, the MSN-NH_2@APE exhibited higher cytotoxicity than the free APE at concentrations between 20 μg mL^{-1} and 80 μg mL^{-1} (Figure 9A). Galactose functionalization of the nanoparticle surface (GMSN@APE in Figure 9A) demonstrated marked enhancement of anticancer activity, especially at low doses (20–40 μg mL^{-1}). Therefore, with an IC_{50} dose of 30.73 ± 3.14 μg mL^{-1}, APE loaded GMSN nanoparticles (GMSN@APE) elicit higher cell death than the free APE (50.9 ± 0.83 μg mL^{-1}) and MSN-NH_2@APE (39.78 ± 1.07 μg mL^{-1}) after 24 h of incubation. This could be attributed to the galactose receptor-mediated enhanced endocytosis of GMSN@APE in comparison with the unmodified nanoparticles and free APE within HepG2 cells. Exposure of the resistant cells (SR5.0-HepG2) to APE also caused the dose-dependent reduction of cell viability (Figure 9C) at concentration between 20 and 100 μg mL^{-1} and revealed an IC_{50} dose of 62.58 ± 2.29 μg mL^{-1}. Cytotoxicity effects of MSN-NH_2@APE nanoparticles treatment on cell viability were higher (IC_{50} 54.61 ± 0.66 μg mL^{-1} vs APE), revealing that nanoparticle encapsulation significantly reduced the viability of SR5.0-HepG2 cell line. Galactose functionalization, on the other hand, again caused a striking decrease of IC_{50} value to 35.64 ± 1.34 μg mL^{-1} (vs MSN-NH_2@APE) as well as cell viability at the APE equivalent doses between 20 μg mL^{-1} and 40 μg mL^{-1}. Versatility of APE and the nanoparticles was further confirmed in Huh-7 cell lines, which have a medium hepatic differentiation rate and a different phenotype than the HepG2 cells.[87] While the IC_{50} dose of crude APE was 42.41 ± 1.88 μg mL^{-1}, the loaded MSN-NH_2 and GMSN displayed 35.25 ± 1.47 μg mL^{-1} (vs APE) and 21.86 ± 0.83 μg mL^{-1} IC_{50} (vs MSN-NH_2@APE) concentrations in Huh-7 cells, respectively (Figure 9E).

Detailed phytochemical analysis revealed that APE contains a mixture of polyphenols and procyanidins. The major constituting compounds such as gallic acid (IC_{50} 69.17 μM), caffeic acid (IC_{50} 1.75 μM) and catechin (IC_{50} 150–200 μg mL^{-1}) have been known to be apoptosis inducers against HepG2 in their individual capacities.[96–98] It is therefore obvious that high levels of procyanidins and polyphenols in the extract could exert a strong cytotoxic effect against HepG2 cells. Encapsulation of the extract in mesoporous silica nanoparticles further increased the effects, probably due to endocytosis and the higher solubility of the extract in the nano-form. This is a common phenomenon related to encapsulation of chemotherapeutics.[99] Moreover, the cytotoxicity studies showcase the advantage of galactose surface modification for the management of sorafenib-resistant liver cancer and their capacity to significantly decrease the dose requirements compared to free extracts.

Interestingly, LDH assay revealed that the extent of cell membrane damage caused by APE, IC_{50} dose (50 μg mL^{-1}), in the normal and SR-HepG2 cells was almost 35% (Figure 9B, D) following a 24 h exposure period, indicating that the extract may have a base line of necrotic activity. The cationic nanoparticle surface is known to irritate the cell membrane through electrostatic stress and can lead to systemic cytotoxicity via necrosis.[100,101] The levels of LDH release remained unchanged ($p > 0.05$) when normal and resistant HepG2 cells were treated with the nanoparticles. In contrast, LDH leakage in the Huh-7 cells was low (7.53 ± 1.89%) in response to the crude APE (Figure 9F). Amine modified nanoparticles (MSN-NH_2@APE) caused a dramatic increase in membrane damage in Huh-7 cells (53.77 ± 5.13%)

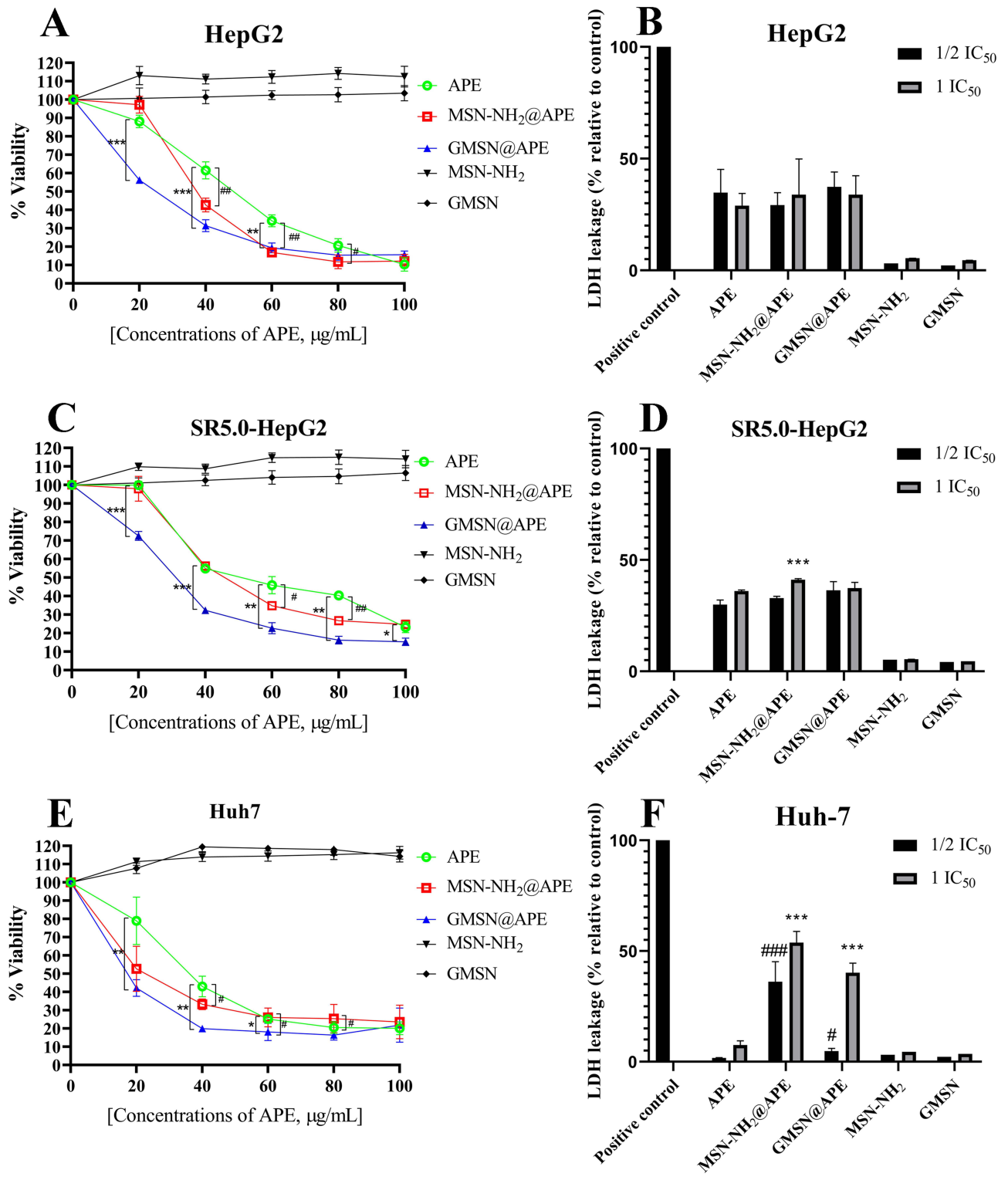

Figure 9 Anticancer activity of APE, MSN-NH2@APE and GMSN@APE on (**A** and **B**) HepG2, (**C** and **D**) SR5.0-HepG2 and (**E** and **F**) Huh-7 cells. Data were expressed as mean ± SD (n = 3); *p < 0.05, **p < 0.01, ***p < 0.001 vs GMSN@APE group; #p < 0.05, ##p < 0.01, ###p < 0.001 vs MSN-NH_2@APE group.

which was higher than the GMSN@APE (40.18 ± 4.35%). This effect was concentration-dependent, in contrast to that observed in HepG2 cells. The differential response of HepG2 and Huh-7 cells is based on the fact that the cells exhibit alterations in their transcriptome and proteome which could affect the influx of a drug into various intracellular

compartments.[102,103] However, it was evident that encapsulated APE induced a certain degree of necrosis in different HCC cell lines as well as in sorafenib-resistant conditions.

Conclusion

Avocado seeds are a rich source of polyphenols and procyanidins. These phytochemicals have been well established as chemotherapeutic agents with multiple tumour-inhibitory mechanisms under drug-resistant conditions. However, their clinical applications remain limited owing to their biopharmaceutical properties and expensive isolation protocols. Our work showed that maceration could be an economical and scalable method for the extraction of anticancer ingredients, including catechin, epicatechin, gallic acid, and caffeic acid, from avocado seeds. The extract demonstrated potential anticancer activity against both non-resistant and sorafenib-resistant HCC cell lines. The delivery of fragile anticancer molecules into the core of the TME remains a challenge for formulation scientists. Mesoporous silica nanoparticles were explored for the first time as viable carriers for APE. We performed selective galactose modification on amino-functionalized mesoporous silica particle surfaces to enhance anticancer activity using a pH-responsive release system. Nanoparticle uptake and endosomal escape capacities appeared prominent in different HCC cell lines, which can enrich drug accumulation at the target sites. APE-loaded MSN offered rapid release to reach therapeutic levels at acidic pH in TME and exhibited significantly higher cytotoxicity in HCC cells than the free extract. Overall, the results suggest that the developed charge-switchable mesoporous silica nanoparticles are potential carriers of plant extracts against drug-resistant HCC. This strategy could also be applied to the encapsulation of other active compounds individually and in bulk for precise delivery to target tumour sites in HCC.

Acknowledgments

This work was supported by the Thailand Science Research and Innovation (TSRI) through Mahidol University (Basic Research Fund: fiscal year 2023, grant number FF-045/2566 (FRB660042/0185)). AB also acknowledges the International Postdoctoral Fellowship received from Mahidol University (fiscal year, 2022).

Author Contributions

Conceptualisation, project design and experimental design, data analysis and evaluation, writing and manuscript editing, P.R.; experimental design, performing experiment-particle synthesis and characterization; writing—original draft preparation, A. B.; experimental design, data analysis and evaluation, plant identification, herbarium processing, plant extraction, O.S.; experimental design, data analysis and evaluation, extract quality control, J.L.; experimental design, data analysis and evaluation, perform experiments – phytochemical analysis, cell toxicity, particle uptake, A.B., A.S., P.P., P.S. and A.C.; experimental design, data analysis and evaluation, phytochemical identification and quantification, P.S. and A.B.; experimental design, data analysis and evaluation, preparation of drug-resistant cell lines, P.R., T.N., K.S., P.N., and A.B. The manuscript was critical reviewed by A.B. P.R. and P.N. All authors made a significant contribution to the work reported, whether that is in the conception, study design, execution, acquisition of data, analysis and interpretation, or in all these areas; All authors took part in revising and reviewing the article; gave final approval of the version to be published; have agreed on the journal to which the article has been submitted; and agree to be accountable for all aspects of the work.

Disclosure

The authors declare no competing interests over the publication of this manuscript.

References

1. Peeters F, Dekervel J. Considerations for individualized first-line systemic treatment in advanced hepatocellular carcinoma. *Curr Opin Pharmacol*. 2023;70:102365. doi:10.1016/j.coph.2023.102365
2. Sherman M. Limitations of screening for hepatocellular carcinoma. *Hepatic Oncol*. 2014;1(2):161–163. doi:10.2217/hep.13.22
3. Y-N L, Shi X, Sun D, et al. Delivery of melarsoprol using folate-targeted PEGylated cyclodextrin-based nanoparticles for hepatocellular carcinoma. *Int J Pharm*. 2023;636:122791. doi:10.1016/j.ijpharm.2023.122791
4. Zheng W, Feng Y, Bai Y, et al. Proanthocyanidins extracted from grape seeds inhibit the growth of hepatocellular carcinoma cells and induce apoptosis through the MAPK/AKT pathway. *Food Biosci*. 2022;45(April 2021):101337. doi:10.1016/j.fbio.2021.101337

5. Gao Z-X, Zhang Z-S, Qin J, et al. Aucubin enhances the antitumor activity of cisplatin through the inhibition of PD-L1 expression in hepatocellular carcinoma. *Phytomedicine*. 2023;112:154715. doi:10.1016/j.phymed.2023.154715
6. Wang H, Ellipilli S, Lee W-J, et al. Multivalent rubber-like RNA nanoparticles for targeted co-delivery of paclitaxel and MiRNA to silence the drug efflux transporter and liver cancer drug resistance. *J Control Release*. 2021;330:173–184. doi:10.1016/j.jconrel.2020.12.007
7. Gao D-Y, Lin -T-T, Sung Y-C, et al. CXCR4-targeted lipid-coated PLGA nanoparticles deliver sorafenib and overcome acquired drug resistance in liver cancer. *Biomaterials*. 2015;67:194–203. doi:10.1016/j.biomaterials.2015.07.035
8. Ali HS, Boshra MS, El Meteini MS, Shafei AE-S, Matboli M. lncRNA- RP11-156p1.3, novel diagnostic and therapeutic targeting via CRISPR/Cas9 editing in hepatocellular carcinoma. *Genomics*. 2020;112(5):3306–3314. doi:10.1016/j.ygeno.2020.06.020
9. Qi Y, Liu Y, Yu B, et al. A lactose-derived CRISPR/cas9 delivery system for efficient genome editing in vivo to treat orthotopic hepatocellular carcinoma. *Adv Sci*. 2020;7(17). doi:10.1002/advs.202001424
10. Valencia-Hernandez LJ, Wong-Paz JE, Ascacio-Valdés JA, Chávez-González ML, Contreras-Esquivel JC, Aguilar CN. Procyanidins: from agro-industrial waste to food as bioactive molecules. *Foods*. 2021;10(12):3152. doi:10.3390/foods10123152
11. J-M L, Gouda M, El-Din Bekhit A, Y-K H, X-Q Y, Chen J-C. Identification of novel bioactive proanthocyanidins with potent antioxidant and anti-proliferative activities from kiwifruit leaves. *Food Biosci*. 2022;46:101554. doi:10.1016/j.fbio.2022.101554
12. Jimenez-Lopez C, Fraga-Corral M, Carpena M, et al. Agriculture waste valorisation as a source of antioxidant phenolic compounds within a circular and sustainable bioeconomy. *Food Funct*. 2020;11(6):4853–4877. doi:10.1039/D0FO00937G
13. Basu A, Namporn T, Ruenraroengsak P. Critical review in designing plant-based anticancer nanoparticles against hepatocellular carcinoma. *Pharmaceutics*. 2023;15(6):1611. doi:10.3390/pharmaceutics15061611
14. Dabas D, Shegog R, Ziegler G, Lambert J. Avocado (Persea americana) seed as a source of bioactive phytochemicals. *Curr Pharm Des*. 2013;19(34):6133–6140. doi:10.2174/1381612811319340007
15. Alkhalaf MI, Alansari WS, Ibrahim EA, ELhalwagy MEA. Anti-oxidant, anti-inflammatory and anti-cancer activities of avocado (Persea americana) fruit and seed extract. *J King Saud Univ - Sci*. 2019;31(4):1358–1362. doi:10.1016/j.jksus.2018.10.010
16. Abd Elkader AM, Labib S, Taha TF, et al. Phytogenic compounds from avocado (Persea americana L.) extracts; antioxidant activity, amylase inhibitory activity, therapeutic potential of type 2 diabetes. *Saudi J Biol Sci*. 2022;29(3):1428–1433. doi:10.1016/j.sjbs.2021.11.031
17. Lara-Márquez M, Báez-Magaña M, Raymundo-Ramos C, et al. Lipid-rich extract from Mexican avocado (Persea americana var. drymifolia) induces apoptosis and modulates the inflammatory response in Caco-2 human colon cancer cells. *J Funct Foods*. 2020;64:103658. doi:10.1016/j.jff.2019.103658
18. Castañeda R, Cáceres A, Velásquez D, Rodríguez C, Morales D, Castillo A. Medicinal plants used in traditional Mayan medicine for the treatment of central nervous system disorders: an overview. *J Ethnopharmacol*. 2022;283:114746. doi:10.1016/j.jep.2021.114746
19. Dabas D, Elias RJ, Ziegler GR, Lambert JD. In vitro antioxidant and cancer inhibitory activity of a colored avocado seed extract. *Int J Food Sci*. 2019;2019:1–7. doi:10.1155/2019/6509421
20. Wang W, Bostic TR, Gu L. Antioxidant capacities, procyanidins and pigments in avocados of different strains and cultivars. *Food Chem*. 2010;122(4):1193–1198. doi:10.1016/j.foodchem.2010.03.114
21. Zhao B, Sun Y, Wang S, et al. Grape seed procyanidin reversal of P-glycoprotein associated multi-drug resistance via down-regulation of NF-κB and MAPK/ERK mediated YB-1 activity in A2780/T cells. *PLoS One*. 2013;8(8):e71071. doi:10.1371/journal.pone.0071071
22. Badawi N, Teaima M, El-Say K, Attia D, El Nabarawi M, Elmazar M. Pomegranate extract-loaded solid lipid nanoparticles: design, optimization, and in vitro cytotoxicity study. *Int J Nanomed*. 2018;13:1313–1326. doi:10.2147/IJN.S154033
23. Mughees M, Samim M, Sharma Y, Wajid S. Identification of protein targets and the mechanism of the cytotoxic action of Ipomoea turpethum extract loaded nanoparticles against breast cancer cells. *J Mater Chem B*. 2019;7(39):6048–6063. doi:10.1039/C9TB00824A
24. Abo Mansour HE, El-Batsh MM, Badawy NS, Mehanna ET, Mesbah NM, Abo-Elmatty DM. Ginger extract loaded into chitosan nanoparticles enhances cytotoxicity and reduces cardiotoxicity of doxorubicin in hepatocellular carcinoma in mice. *Nutr Cancer*. 2021;73(11–12):2347–2362. doi:10.1080/01635581.2020.1823436
25. Mughees M, Wajid S, Samim M. Cytotoxic potential of Artemisia absinthium extract loaded polymeric nanoparticles against breast cancer cells: insight into the protein targets. *Int J Pharm*. 2020;586:119583. doi:10.1016/j.ijpharm.2020.119583
26. Shabestarian H, Homayouni Tabrizi M, Movahedi M, Neamati A, Sharifnia F. Putative mechanism for cancer suppression by PLGA nanoparticles loaded with Peganum harmala smoke extract. *J Microencapsul*. 2021;38(5):324–337. doi:10.1080/02652048.2021.1917715
27. Cui L, Liu W, Liu H, et al. pH-triggered charge-reversal mesoporous silica nanoparticles stabilized by chitosan oligosaccharide/carboxymethyl chitosan hybrids for effective intracellular delivery of doxorubicin. *ACS Appl Bio Mater*. 2019;2(5):1907–1919. doi:10.1021/acsabm.8b00830
28. Tang F, Li L, Chen D. Mesoporous silica nanoparticles: synthesis, biocompatibility and drug delivery. *Adv Mater*. 2012;24(12):1504–1534. doi:10.1002/adma.201104763
29. Priya V, Mehata AK, Jain D, Singh SK, Muthu MS, Muthu MS. Efficient delivery of Abciximab using mesoporous silica nanoparticles: in-vitro assessment for targeted and improved antithrombotic activity. *Colloids Surf B Biointerfaces*. 2022;218(July):112697. doi:10.1016/j.colsurfb.2022.112697
30. Lohiya G, Katti DS. Carboxylated chitosan-mediated improved efficacy of mesoporous silica nanoparticle-based targeted drug delivery system for breast cancer therapy. *Carbohydr Polym*. 2022;277(August 2021):118822. doi:10.1016/j.carbpol.2021.118822
31. Kim D, Byun J, Kim SI, et al. DNA-cloaked nanoparticles for tumor microenvironment-responsive activation. *J Control Release*. 2022;350:448–459. doi:10.1016/j.jconrel.2022.08.044
32. Xu Q, Lan X, Lin H, et al. Tumor microenvironment-regulating nanomedicine design to fight multi-drug resistant tumors. *WIREs Nanomedi Nanobiotechnology*. 2023;15(1). doi:10.1002/wnan.1842
33. Ganguly SS, Dewanjee S, Sen R, et al. Apigenin-loaded galactose tailored PLGA nanoparticles: a possible strategy for liver targeting to treat hepatocellular carcinoma. *Colloids Surf B Biointerfaces*. 2021;204:111778. doi:10.1016/j.colsurfb.2021.111778
34. Liu L, Zong Z-M, Liu Q, et al. A novel galactose-PEG-conjugated biodegradable copolymer is an efficient gene delivery vector for immunotherapy of hepatocellular carcinoma. *Biomaterials*. 2018;184:20–30. doi:10.1016/j.biomaterials.2018.08.064
35. Zou Y, Song Y, Yang W, Meng F, Liu H, Zhong Z. Galactose-installed photo-crosslinked pH-sensitive degradable micelles for active targeting chemotherapy of hepatocellular carcinoma in mice. *J Control Release*. 2014;193:154–161. doi:10.1016/j.jconrel.2014.05.016

36. Quan S, Wang Y, Zhou A, Kumar P, Narain R. Galactose-based thermosensitive nanogels for targeted drug delivery of iodoazomycin arabinofuranoside (IAZA) for theranostic management of hypoxic hepatocellular carcinoma. *Biomacromolecules*. 2015;16(7):1978–1986. doi:10.1021/acs.biomac.5b00576
37. Fan N, Zhao J, Zhao W, et al. Celastrol-loaded lactosylated albumin nanoparticles attenuate hepatic steatosis in non-alcoholic fatty liver disease. *J Control Release*. 2022;347:44–54. doi:10.1016/j.jconrel.2022.04.034
38. Mal A, Prabhuraj RS, Malhotra R, et al. pH-responsive sustained delivery of doxorubicin using aminated and PEGylated mesoporous silica nanoparticles leads to enhanced antitumor efficacy in pre-clinical orthotopic breast cancer model. *J Drug Deliv Sci Technol*. 2022;77 (September). doi:10.1016/j.jddst.2022.103800
39. Mukherjee MB, Mullick R, Reddy BU, Das S, Raichur AM. Galactose functionalized mesoporous silica nanoparticles as delivery vehicle in the treatment of hepatitis c infection. *ACS Appl Bio Mater*. 2020;3(11):7598–7610. doi:10.1021/acsabm.0c00814
40. Quan G, Pan X, Wang Z, et al. Lactosaminated mesoporous silica nanoparticles for asialoglycoprotein receptor targeted anticancer drug delivery. *J Nanobiotechnology*. 2015;13(1):7. doi:10.1186/s12951-015-0068-6
41. Radovic-Moreno AF, Lu TK, Puscasu VA, Yoon CJ, Langer R, Farokhzad OC. Surface charge-switching polymeric nanoparticles for bacterial cell wall-targeted delivery of antibiotics. *ACS Nano*. 2012;6(5):4279–4287. doi:10.1021/nn3008383
42. Sithisarn P, Rojsanga P, Sithisarn P, Kongkiatpaiboon S. Antioxidant activity and antibacterial effects on clinical isolated streptococcus suis and staphylococcus intermedius of extracts from several parts of cladogynos orientalis and their phytochemical screenings. *Evid Based Complement Altern Med*. 2015;2015:1–9. doi:10.1155/2015/908242
43. Payne MJ, Hurst WJ, Stuart DA, et al. Determination of total procyanidins in selected chocolate and confectionery products using DMAC. *J AOAC Int*. 2010;93(1):89–96.
44. Department of medical sciences m of ph. Thai herbal pharmacopoeia ii supplement. 2020. Available from: https://www.bdn.go.th/tp/ebook. Accessed March 29, 2024.
45. Yang Y, Lin Y, Di D, et al. Gold nanoparticle-gated mesoporous silica as redox-triggered drug delivery for chemo-photothermal synergistic therapy. *J Colloid Interface Sci*. 2017;508:323–331. doi:10.1016/j.jcis.2017.08.050
46. Ramírez M, de Los Á, Bindini E, et al. Impact of PEGylation on the degradation and pore organization in mesoporous silica nanoparticles: a study of the inner mesoporous structure in physiologically relevant ionic conditions. *Colloids Surf B Biointerfaces*. 2022;219:112797. doi:10.1016/j.colsurfb.2022.112797
47. Brunauer S, Emmett PH, Teller E. Adsorption of gases in multimolecular layers. *J Am Chem Soc*. 1938;60(2):309–319. doi:10.1021/ja01269a023
48. Bardestani R, Patience GS, Kaliaguine S. Experimental methods in chemical engineering: specific surface area and pore size distribution measurements—BET, BJH, and DFT. *Can J Chem Eng*. 2019;97(11):2781–2791. doi:10.1002/cjce.23632
49. El-Marakby EM, Hathout RM, Taha I, Mansour S, Mortada ND. A novel serum-stable liver targeted cytotoxic system using valerate-conjugated chitosan nanoparticles surface decorated with glycyrrhizin. *Int J Pharm*. 2017;525(1):123–138. doi:10.1016/j.ijpharm.2017.03.081
50. Wu D, Shi X, Zhao F, et al. An injectable and tumor-specific responsive hydrogel with tissue-adhesive and nanomedicine-releasing abilities for precise locoregional chemotherapy. *Acta Biomater*. 2019;96:123–136. doi:10.1016/j.actbio.2019.06.033
51. Lee WE, Besnier M, Genetzakis E, et al. High-throughput measure of mitochondrial superoxide levels as a marker of coronary artery disease to accelerate drug translation in patient-derived endothelial cells using Opera Phenix® technology. *Int J Mol Sci*. 2023;25(1):22. doi:10.3390/ijms25010022
52. Dong K, Wang Z, Zhang Y, Ren J, Qu X. Metal–Organic Framework-Based Nanoplatform for Intracellular Environment-Responsive Endo/Lysosomal Escape and Enhanced Cancer Therapy. *ACS Appl Mater Interfaces*. 2018;10(38):31998–32005. doi:10.1021/acsami.8b11972
53. Nagahama K, Utsumi T, Kumano T, Maekawa S, Oyama N, Kawakami J. Discovery of a new function of curcumin which enhances its anticancer therapeutic potency. *Sci Rep*. 2016;6(1):30962. doi:10.1038/srep30962
54. Soledad CT, Paola H, Carlos Enrique O-V, Israel RI, GuadalupeVirginia N-M, Á R. Avocado seeds (Persea americana cv. Criollo sp.): lipophilic compounds profile and biological activities. *Saudi J Biol Sci*. 2021;28(6):3384–3390. doi:10.1016/j.sjbs.2021.02.087
55. Hatzakis E, Mazzola EP, Shegog RM, Ziegler GR, Lambert JD. Perseorangin: a natural pigment from avocado (Persea americana) seed. *Food Chem*. 2019;293(April):15–22. doi:10.1016/j.foodchem.2019.04.064
56. Stojiljković D, Arsić I, Tadić V. Extracts of wild apple fruit (Malus sylvestris (L.) Mill. Rosaceae) as a source of antioxidant substances for use in production of nutraceuticals and cosmeceuticals. *Ind Crops Prod*. 2016;80:165–176. doi:10.1016/j.indcrop.2015.11.023
57. Tanaka Y, Tsuneoka M. Gallic acid derivatives propyl gallate and epigallocatechin gallate reduce rRNA transcription via induction of KDM2A activation. *Biomolecules*. 2021;12(1):30. doi:10.3390/biom12010030
58. Cedó L, Castell-Auví A, Pallarès V, et al. Gallic acid is an active component for the anticarcinogenic action of grape seed procyanidins in pancreatic cancer cells. *Nutr Cancer*. 2014;66(1):88–96. doi:10.1080/01635581.2014.851714
59. S-H W, Mou C-Y, Lin H-P. Synthesis of mesoporous silica nanoparticles. *Chem Soc Rev*. 2013;42(9):3862. doi:10.1039/c3cs35405a
60. Hoffmann F, Cornelius M, Morell J, Fröba M. Silica-based mesoporous organic–inorganic hybrid materials. *Angew Chem Int Ed*. 2006;45 (20):3216–3251. doi:10.1002/anie.200503075
61. Lartigue L, Innocenti C, Kalaivani T, et al. Water-dispersible sugar-coated iron oxide nanoparticles. an evaluation of their relaxometric and magnetic hyperthermia properties. *J Am Chem Soc*. 2011;133(27):10459–10472. doi:10.1021/ja111448t
62. da Silva AC, Cordeiro P, Estevão B, et al. Synthesis of highly ordered mesoporous MCM-41: selective external functionalization by time control. *J Braz Chem Soc*. 2019. doi:10.21577/0103-5053.20190058
63. Nguyen CH, Fu -C-C, Chen Z-H, Van Tran TT, Liu S-H, Juang R-S. Enhanced and selective adsorption of urea and creatinine on amine-functionalized mesoporous silica SBA-15 via hydrogen bonding. *Microporous Mesoporous Mater*. 2021;311:110733. doi:10.1016/j.micromeso.2020.110733
64. Krajewska K, Gołkowska AM, Nowak M, et al. Molecular level characterisation of the surface of carbohydrate-functionalised mesoporous silica nanoparticles (MSN) as a potential targeted drug delivery system via high resolution magic angle spinning (HR-MAS) NMR spectroscopy. *Int J Mol Sci*. 2022;23(11):5906. doi:10.3390/ijms23115906
65. Pimentel-Moral S, Teixeira MC, Fernandes AR, et al. Polyphenols-enriched hibiscus sabdariffa extract-loaded nanostructured lipid carriers (NLC): optimization by multi-response surface methodology. *J Drug Deliv Sci Technol*. 2019;49:660–667. doi:10.1016/j.jddst.2018.12.023

66. Maitra B, Halima Khatun M, Ahmed F, et al. Biosynthesis of bixa orellana seed extract mediated silver nanoparticles with moderate antioxidant, antibacterial and antiproliferative activity. *Arab J Chem*. 2023;16(5):104675. doi:10.1016/j.arabjc.2023.104675
67. Schmidt LM, Dos Santos J, de Oliveira TV, et al. Drug-loaded mesoporous silica on carboxymethyl cellulose hydrogel: development of innovative 3D printed hydrophilic films. *Int J Pharm*. 2022;620:121750. doi:10.1016/j.ijpharm.2022.121750
68. Ghosh N, Kundu M, Ghosh S, et al. pH-responsive and targeted delivery of chrysin via folic acid-functionalized mesoporous silica nanocarrier for breast cancer therapy. *Int J Pharm*. 2023;631:122555. doi:10.1016/j.ijpharm.2022.122555
69. Su S, Hao L, Chen H, Zhou X, Zhou H. Salicylaldehyde and D-(+)-galactose functionalized chitosan oligosaccharide nanoparticles as carriers for sustained release of pesticide with enhanced UV stability. *Colloids Surf a Physicochem Eng Aspects*. 2023;656:130437. doi:10.1016/j.colsurfa.2022.130437
70. Mokhtari S, Solati-Hashjin M, Khosrowpour Z, Gholipourmalekabadi M. Layered double hydroxide-galactose as an excellent nanocarrier for targeted delivery of curcumin to hepatocellular carcinoma cells. *Appl Clay Sci*. 2021;200:105891. doi:10.1016/j.clay.2020.105891
71. Margarida Cardoso M, Peça IN, Raposo CD, et al. Doxorubicin-loaded galactose-conjugated poly(d,l-lactide-co-glycolide) nanoparticles as hepatocyte-targeting drug carrier. *J Microencapsul*. 2016;33(4):315–322. doi:10.1080/02652048.2016.1185474
72. Schneider P. Adsorption isotherms of microporous-mesoporous solids revisited. *Appl Catal a Gen*. 1995;129(2):157–165. doi:10.1016/0926-860X(95)00110-7
73. Sonwane CG, Bhatia SK. Determination of pore size distribution of mesoporous materials by regularization. *Stud Surf Sci Catal*. 2000;129:607–615. doi:10.1016/s0167-2991(00)80263-3
74. Sing KSW. Adsorption methods for the characterization of porous materials. *Adv Colloid Interface Sci*. 1998;76-77:3–11. doi:10.1016/S0001-8686(98)00038-4
75. Montiel-Centeno K, Barrera D, García-Villén F, et al. Cephalexin loading and controlled release studies on mesoporous silica functionalized with amino groups. *J Drug Deliv Sci Technol*. 2022;72:103348. doi:10.1016/j.jddst.2022.103348
76. Chen X, Wu Y, Li R, et al. Galactose-modified nanoparticles for delivery of microRNA to mitigate the progress of abdominal aortic aneurysms via regulating macrophage polarization. *Nanomedicine Nanotechnology, Biol Med*. 2022;44:102564. doi:10.1016/j.nano.2022.102564
77. Basu A, Kundu S, Basu C, Ghosh SK, Sur R, Mukherjee A. Biopolymer nanoparticle surface chemistry dictates the nature and extent of protein hard Corona. *J Mol Liq*. 2019;282:169–176. doi:10.1016/j.molliq.2019.03.016
78. Guo Z, Sui J, Ma M, et al. pH-Responsive charge switchable PEGylated ε-poly-l-lysine polymeric nanoparticles-assisted combination therapy for improving breast cancer treatment. *J Control Release*. 2020;326:350–364. doi:10.1016/j.jconrel.2020.07.030
79. Chen J, Dai Y, Gong X, Zhang G. Cation-amino acid interactions: implications for protein destabilization. *Biochem Biophys Res Commun*. 2021;548:47–52. doi:10.1016/j.bbrc.2021.02.017
80. Wen M, Li Y, Zhong W, et al. Interactions of cationic gold nanoclusters with serum proteins and effects on their cellular responses. *J Colloid Interface Sci*. 2022;610:116–125. doi:10.1016/j.jcis.2021.12.044
81. Ruenraroengsak P, Novak P, Berhanu D, et al. Respiratory epithelial cytotoxicity and membrane damage (holes) caused by amine-modified nanoparticles. *Nanotoxicology*. 2012;6(1):94–108. doi:10.3109/17435390.2011.558643
82. Yang J, Liu S, Ye Z, Deng L, Dong A, Zhang J. Multi-transformable nanocarrier with tumor extracellular acidity-activated charge reversal, size reduction and ligand reemergence for in vitro efficient doxorubicin loading and delivery. *Mater Sci Eng C*. 2020;116:111250. doi:10.1016/j.msec.2020.111250
83. Kim M-K, D-H K, Y-G N, et al. Optimization of mesoporous silica nanoparticles through statistical design of experiment and the application for the anticancer drug. *Pharmaceutics*. 2021;13(2):184. doi:10.3390/pharmaceutics13020184
84. Croissant JG, Zhang D, Alsaiari S, et al. Protein-gold clusters-capped mesoporous silica nanoparticles for high drug loading, autonomous gemcitabine/doxorubicin co-delivery, and in-vivo tumor imaging. *J Control Release*. 2016;229:183–191. doi:10.1016/j.jconrel.2016.03.030
85. Pattnaik S, Pathak K. Mesoporous silica molecular sieve based nanocarriers: transpiring drug dissolution research. *Curr Pharm Des*. 2017;23(3):467–480. doi:10.2174/1381612822666161026162005
86. Lou S, Gao S, Wang W, et al. Galactose-functionalized multi-responsive nanogels for hepatoma-targeted drug delivery. *Nanoscale*. 2015;7(7):3137–3146. doi:10.1039/C4NR06714B
87. Cavallaro G, Farra R, Craparo EF, et al. Galactosylated polyaspartamide copolymers for siRNA targeted delivery to hepatocellular carcinoma cells. *Int J Pharm*. 2017;525(2):397–406. doi:10.1016/j.ijpharm.2017.01.034
88. Liu X, Han M, Xu J, et al. Asialoglycoprotein receptor-targeted liposomes loaded with a norcantharimide derivative for hepatocyte-selective targeting. *Int J Pharm*. 2017;520(1–2):98–110. doi:10.1016/j.ijpharm.2017.02.010
89. Kabir TD, Ganda C, Brown RM, et al. A microRNA-7/growth arrest specific 6/TYRO3 axis regulates the growth and invasiveness of sorafenib-resistant cells in human hepatocellular carcinoma. *Hepatology*. 2018;67(1):216–231. doi:10.1002/hep.29478
90. Chen J, Li J, Zhou J, et al. Metal–phenolic coatings as a platform to trigger endosomal escape of nanoparticles. *ACS Nano*. 2019;13(10):11653–11664. doi:10.1021/acsnano.9b05521
91. Gisbert-Garzarán M, Lozano D, Matsumoto K, et al. Designing mesoporous silica nanoparticles to overcome biological barriers by incorporating targeting and endosomal escape. *ACS Appl Mater Interfaces*. 2021;13(8):9656–9666. doi:10.1021/acsami.0c21507
92. Beach MA, Teo SLY, Chen MZ, et al. Quantifying the endosomal escape of pH-responsive nanoparticles using the split luciferase endosomal escape quantification assay. *ACS Appl Mater Interfaces*. 2022;14(3):3653–3661. doi:10.1021/acsami.1c18359
93. Kandil R, Xie Y, Heermann R, et al. Coming in and finding out: blending receptor-targeted delivery and efficient endosomal escape in a novel bio-responsive siRNA delivery system for gene knockdown in pulmonary T cells. *Adv Ther*. 2019;2(7). doi:10.1002/adtp.201900047
94. Mejia F, Khan S, Bilgicer B. Liposomal targeting modifies endosomal escape: design and mechanistic implications. *ACS Biomater Sci Eng*. 2022;8(3):1067–1073. doi:10.1021/acsbiomaterials.2c00100
95. Hussein NA, Malla S, Pasternak MA, et al. The role of endolysosomal trafficking in anticancer drug resistance. *Drug Resist Updat*. 2021;57:100769. doi:10.1016/j.drup.2021.100769
96. Abd-Rabou AA, Ahmed HH. CS-PEG decorated PLGA nano-prototype for delivery of bioactive compounds: a novel approach for induction of apoptosis in HepG2 cell line. *Adv Med Sci*. 2017;62(2):357–367. doi:10.1016/j.advms.2017.01.003

97. Raviadaran R, Ng MH, Chandran D, Ooi KK, Manickam S. Stable W/O/W multiple nanoemulsion encapsulating natural tocotrienols and caffeic acid with cisplatin synergistically treated cancer cell lines (A549 and HEP G2) and reduced toxicity on normal cell line (HEK 293). *Mater Sci Eng C*. 2021;121:111808. doi:10.1016/j.msec.2020.111808
98. Jain P, Kumar N, Josyula VR, et al. A study on the role of (+)-catechin in suppression of HepG2 proliferation via caspase dependent pathway and enhancement of its in vitro and in vivo cytotoxic potential through liposomal formulation. *Eur J Pharm Sci*. 2013;50(3–4):353–365. doi:10.1016/j.ejps.2013.08.005
99. Soo E, Thakur S, Qu Z, Jambhrunkar S, Parekh HS, Popat A. Enhancing delivery and cytotoxicity of resveratrol through a dual nanoencapsulation approach. *J Colloid Interface Sci*. 2016;462:368–374. doi:10.1016/j.jcis.2015.10.022
100. Yim H, Park S, Bae YH, Na K. Biodegradable cationic nanoparticles loaded with an anticancer drug for deep penetration of heterogeneous tumours. *Biomaterials*. 2013;34(31):7674–7682. doi:10.1016/j.biomaterials.2013.06.058
101. An M, Yu C, Xi J, et al. Induction of necrotic cell death and activation of STING in the tumor microenvironment via cationic silica nanoparticles leading to enhanced antitumor immunity. *Nanoscale*. 2018;10(19):9311–9319. doi:10.1039/C8NR01376D
102. Qiu G-H, Xie X, Xu F, Shi X, Wang Y, Deng L. Distinctive pharmacological differences between liver cancer cell lines HepG2 and Hep3B. *Cytotechnology*. 2015;67(1):1–12. doi:10.1007/s10616-014-9761-9
103. Guo L, Dial S, Shi L, et al. Similarities and differences in the expression of drug-metabolizing enzymes between human hepatic cell lines and primary human hepatocytes. *Drug Metab Dispos*. 2011;39(3):528–538. doi:10.1124/dmd.110.035873